

# STAR FORMATION AND THE INTERSTELLAR MEDIUM IN NEARBY TIDAL STREAMS (SAINTS): SPITZER MID-INFRARED SPECTROSCOPY AND IMAGING OF INTERGALACTIC STAR-FORMING OBJECTS

S. J. U. Higdon<sup>1</sup>, J. L. Higdon<sup>1</sup>, B. J. Smith<sup>2</sup>, AND M. Hancock<sup>3</sup>

## ABSTRACT

A spectroscopic analysis of 10 intergalactic star forming objects (ISFOs) and a photometric analysis of 67 ISFOs in a sample of 14 interacting systems is presented. The majority of the ISFOs have relative polycyclic aromatic hydrocarbon (PAH) band strengths similar to those of nearby spiral and starburst galaxies. In contrast to what is observed in blue compact dwarfs (BCDs) and local giant HII regions in the Milky Way (NGC 3603) and the Magellanic Clouds (30 Doradus and N 66), the relative PAH band strengths in ISFOs correspond to models with a significant PAH ion fraction ( $< 50\%$ ) and bright emission from large PAHs ( $\sim 100$  carbon atoms). The  $[\text{Ne III}]/[\text{Ne II}]$  and  $[\text{S IV}]/[\text{S III}]$  line flux ratios indicate moderate levels of excitation with an interstellar radiation field that is harder than the majority of the Spitzer Infrared Nearby Galaxies Survey and starburst galaxies, but softer than BCDs and local giant HII regions. The ISFO neon line flux ratios are consistent with a burst of star formation  $\lesssim 6$  million years ago. Most of the ISFOs have  $\sim 10^6 M_{\odot}$  of warm  $\text{H}_2$  with a likely origin in photo-dissociation regions (PDRs). Infrared Array Camera photometry shows the ISFOs to be bright at  $8 \mu\text{m}$ , with one third having  $[4.5] - [8.0] > 3.7$ , i.e., enhanced non-stellar emission, most likely due to PAHs, relative to normal spirals, dwarf irregulars and BCD galaxies. The relative strength of the  $8 \mu\text{m}$  emission compared to that at  $3.6 \mu\text{m}$  or  $24 \mu\text{m}$  separates ISFOs from dwarf galaxies in Spitzer two color diagrams. The infrared power in two thirds of the ISFOs is dominated by emission from grains in a diffuse interstellar medium. One in six ISFOs have significant emission from PDRs, contributing  $\sim 30\% - 60\%$  of the total power. ISFOs are young knots of intense star formation.

---

<sup>1</sup>Physics Department, Georgia Southern University, Statesboro, GA 30460, USA

<sup>2</sup>Department of Physics and Astronomy, East Tennessee State University, Johnson City, TN 37614, USA

<sup>3</sup>Bishop Gorman High School, 5959 Hualapai Way, Las Vegas, NV 89148, USA

*Subject headings:* galaxies: dwarf — galaxies: formation, galaxies: individual (Arp 72, Arp 84, Arp 87, Arp 105, Arp 242, Arp 284, Stephan’s Quintet, NGC 5291) — galaxies: interactions — infrared: galaxies

## 1. INTRODUCTION

In addition to triggering starbursts, mergers of dusty, gas rich disk galaxies frequently lead to the formation of tidal tails that can stretch many disk diameters from the site of the collision (Toomre & Toomre 1972; Schweizer 1978; Sanders & Mirabel 1996). These structures are typically HI rich with blue UV/optical color, reflecting both their origin in the outer spiral disk and on-going star formation (van der Hulst 1979; Schombert et al. 1990; Mirabel et al. 1991; Hibbard & van Gorkom 1996, Smith et al. 2010). Zwicky (1956) proposed that dwarf galaxies might form out of self-gravitating clumps within tidal tails, and indeed, concentrations of gas and star forming regions are commonly found there, with HI masses and optical luminosities comparable with dwarf galaxies. A wide range in HI masses have been derived for these objects, from  $3 \times 10^8 M_\odot$  for the HI condensations in NGC 7252’s plumes (Hibbard et al. 1994) to  $\approx 10^{10} M_\odot$  in NGC 5291 (Duc & Mirabel 1998), with  $\approx 10^9 M_\odot$  being typical (e.g., Duc & Mirabel 1994; Hibbard & van Gorkom 1996).

In this paper we use the broad term “intergalactic star forming object” (ISFO), recognizing that some of them may formed as a result of tidal interactions between the parent galaxies, others from ram-sweeping of debris material, or inflow of material, or the interplay of more than one of these physical processes. These ISFOs range in mass from super star clusters ( $10^4 - 10^6 M_\odot$ ) to tidal dwarf galaxies (TDGs;  $\gtrsim 10^9 M_\odot$ ). The bound ISFOs will become bona-fide TDGs or intergalactic clusters. Many ISFOs and their associated tidal streams may be accreted back onto the parent galaxy, possibly triggering further star formation in the disk. Leftover material will enrich the intergalactic medium with metals and dust (Morris & van den Bergh 1994). The fraction of ISFOs that are gravitationally bound and long-lived is still an open question (e.g., Hibbard & Mihos 1995, Bournaud & Duc 2006, Duc et al. 2014). Kaviraj et al. (2012) analysed data from a sample of mergers observed as part of the Sloan Digital Sky Survey, and concluded that  $\sim 6\%$  of dwarfs in nearby clusters have a tidal origin. In contrast, Hunsberger et al. (1996) concluded that TDGs may make up 30% - 50% of the dwarf galaxy population in compact groups. Observations with high spatial and velocity resolution are necessary to confirm that a ISFO is a physical condensation, and not just a chance alignment of material along our line of sight. Ideally a rotation curve will be constructed to determine whether the ISFO is gravitationally bound, i.e., a bona-fide tidal dwarf galaxy. These observations are generally beyond, or at the limits of the current

observatories.

Here we are studying ISFOs to look for insights into star formation that is influenced by an external event, i.e., interacting systems. Computer simulations by Elmegreen et al. (1993) showed that gas properties play a key role in the formation of TDGs. The elevated velocity dispersion in the tidal stream leads to an increase in the Jeans mass resulting in massive clouds which may be more stable and long-lived. TDGs are formed from gas stripped from the outer portions of the parent galaxy disk. This material has a higher metallicity (e.g., the two TDGs in NGC 5291 have  $\log(\text{O}/\text{H}) + 12 = 8.4$ ; Longmore et al. 1979; Pena et al. 1991; Duc & Mirabel 1998) than the gas found in isolated low-metallicity dwarfs hence the threshold HI column density for star formation may be lower in TDGs. A typical dynamical timescale is  $\sim 10^8$  yr for the formation of condensations at the tips of tidal tails, indicating that any young stellar population has been formed in situ, and has not simply been stripped from the disk of the progenitor galaxy along with the older stars, gas and dust (Elmegreen et al. 1993). A luminous ISFO at the base of a tidal feature, referred to as a “hinge clump” (e.g., Hancock et al. 2007) may be produced by orbit crowding in the tidal feature (e.g., Struck & Smith 2012). Additional ISFOs can be distributed in a seemingly random pattern or distributed more regularly, in a “beads-on-a-string” structure, which is a hallmark of large scale gravitational instability (e.g., Elmegreen & Efremov 1996, Hancock et al. 2007).

Earlier observations have shown that the mid-infrared spectra of ISFOs are rich in atomic and molecular features from the ISM, including fine structure lines such as [Ne II]  $12.81 \mu\text{m}$ , [Ne III]  $15.56 \mu\text{m}$ , polycyclic aromatic hydrocarbons (PAHs) and warm molecular hydrogen (Higdon, Higdon & Marshal 2006b, hereafter HHM06). The mid-infrared spectra of star-forming dwarf galaxies are known to differ substantially from those of spirals, with weaker PAH emission and higher [Ne III]/[Ne II] line ratios (e.g., Thuan et al. 1999; Madden 2000; Galliano et al. 2003; Houck et al. 2004a; Madden et al. 2006; Hunt et al. 2010). The higher [Ne III]/[Ne II] ratio is a consequence of the lower metallicity (stars are hotter and dust absorption is lower) resulting in harder ultraviolet interstellar radiation fields (ISRFs). The weaker PAH features in dwarfs may also be due to metallicity, either directly as a result of the paucity of available enriched raw material to build the PAHs or an indirect consequence of the harder UV field. PAHs can be destroyed in hard UV fields (Plante & Sauvage 2002; Gordon et al. 2008), while young systems may not have the low mass asymptotic giant branch (AGB) stars to create PAH precursors in the interstellar medium (e.g., Galliano et al. 2008). Hard ISRFs may preferentially destroy smaller PAHs, leading to larger PAHs on average in dwarf galaxies, as indicated by the relative strengths of the different mid-infrared PAH features in blue compact dwarfs (BCDs; Hunt et al. 2010). Extreme low metallicity systems have a paucity of PAHs and a hard ISRF, but other factors in the physical environment may drive the relative PAH strengths in more enriched environments.

It is unknown whether the mid-infrared spectra of most tidal features more closely resemble the global spectra of spiral galaxies or those of dwarf galaxies, since only a handful have been studied in detail with the Spitzer Infrared Spectrograph (IRS, Houck et al. 2004b; e.g., HHM06, Higdon & Higdon 2008, Higdon et al. 2010). Tidal features tend to have lower metallicities than the average values for inner disks of spirals, thus may be expected to have weaker PAH features. However, tidal structures tend to have higher metallicities on average than classical dwarfs with the same luminosity (e.g., Weilbacher et al. 2003; de Mello et al. 2012). For example, the spectra of the TDGs in NGC 5291 show prominent PAH features (HHM06).

Since the PAH features contribute significantly to the broadband  $8\ \mu\text{m}$  flux as measured by the Spitzer Infrared Array Camera (IRAC, Fazio et al. 2004b), their emission directly affects the IRAC colors of galaxies. Low metallicity dwarfs tend to be deficient in  $8\ \mu\text{m}$  flux due to weak PAH emission relative to the underlying continuum (e.g., Engelbracht et al. 2005, Rosenberg et al. 2006, 2008, Draine et al. 2007, Madden et al. 2006, Wu et al. 2007). ISFOs in NGC 5291 tend to have red Spitzer  $[4.5] - [8.0]$  colors (HHM06). This may be due to higher mass-normalized star formation rates and lower proportions of underlying older stars.

Here we investigate the Spitzer spectral properties of a set of 10 ISFOs and present a photometric analysis of a larger sample of 67 ISFOs. In Section 2 we describe our sample selection. In Section 3 we describe the observations and data analysis. The results are used in Section 4 to address these key questions pertaining to the properties of ISFOs:

*1) Are the relative PAH strengths best matched to models with bright emission from small or large PAHs? 2) are the PAHs mainly neutral or charged? 3) Are the interstellar radiation fields (ISRF) hard? 4) How much warm molecular gas do the ISFOs contain? 5) Can ISFOs be identified by their mid-infrared colors? 6) Does the bulk of the infrared emission arise in dust illuminated by a diffuse ISRF or by dust embedded in intense fields associated with photo-dissociation regions (PDRs)?*

While addressing each question we compare the results for the ISFOs to the global properties of different galaxy types (starburst, spirals and BCDs) and also to individual sources in three local giant HII regions, NGC 3603 in the Milky Way, 30 Doradus (hereafter 30 Dor.) in the Large Magellanic Cloud (LMC), and N 66 in the Small Magellanic Cloud (SMC) and knots of star formation in the disks of nearby interacting galaxies. Our findings are summarized in Section 5.

## 2. THE SAMPLE

The ISFO sample was derived from 12 systems showing clear signs of recent or on-going gravitational interactions as evidenced by highly extended optical tails and/or bridges, plus two additional systems with more complex interaction histories (NGC 5291/Seashell and Stephans Quintet) with known ISFO populations. These are shown in Figure 1 and the 14 systems are briefly described in the figure captions. We purposely chose relatively nearby systems in order to distinguish individual ISFOs within a given tidal feature subject to the angular resolution constraints of IRAC and Multiband Imaging Photometer (MIPS). Our intent is to identify a sufficiently large sample of ISFOs in order to derive basic properties of the population, rather than conduct a survey of every known system with tails/plumes. The targets were originally observed as part of Spitzer programs Tidal Dwarf Galaxies (Program name SJH-TDGS; HHM06, Higdon & Higdon 2008), Spiral Bridges and Tails (Program name SB&T; Smith et al. 2007a, 2008, 2010, Hancock et al. 2007) and Star Formation and the ISM in Nearby Tidal Streams (Program name SAINTS; Higdon et al. 2010). Candidate selection was made using the  $3.6\mu\text{m}$  and  $8\mu\text{m}$  images. This is discussed in Section 3.1. Our sample consists of 67 ISFOs, which we list in Table 1. Their distances are assumed to be that of their parent galaxies which are taken from the literature, and range from 28-140 Mpc, with a corresponding spatial scale of  $136\text{-}678\text{ pc arcsec}^{-1}$ .

The ISFOs in our spectral sample with published metallicities have values of one third solar or higher: NGC 5291 N and NGC 5291 S with  $\log(\text{O}/\text{H}) +12 = 8.4$  (Longmore et al. 1979; Pena et al. 1991; Duc & Mirabel 1998); Arp 72 with  $\log(\text{O}/\text{H}) +12 = 8.7$  (Smith et al. 2010); Arp 105S with  $\log(\text{O}/\text{H}) +12 = 8.4$  and Arp 105N with  $\log(\text{O}/\text{H}) +12 = 8.6$  (Duc & Mirabel 1994; and Arp 245 with  $\log(\text{O}/\text{H}) +12 \sim 8.65$  (Duc et al. 2000).

Ten ISFOs from this list with  $F_{8\mu\text{m}} \gtrsim 1\text{ mJy}$  were observed with the IRS: Arp 72-S1, Arp 82-N1, Arp 84-N1, Arp 87-N1 (Higdon et al. 2010), Ambartzumian’s knot (Arp 105-S2, Higdon & Higdon 2008, Boquien et al. 2009), Arp 242-N3 in The Mice (Higdon et al. 2010), Arp 284-SW, SQ-A in Stephan’s Quintet (Higdon & Higdon 2008, Higdon et al. 2010), and TDG N and S in NGC 5291 (HHM06).

## 3. OBSERVATIONS AND DATA ANALYSIS

### 3.1. Spitzer Photometry

Infrared images for the majority of the sample were obtained as part of our earlier programs. The IRAC  $3.6\mu\text{m}$ ,  $4.5\mu\text{m}$ ,  $5.8\mu\text{m}$  and  $8\mu\text{m}$  data for NGC 5291 were presented

in HHM06; for Stephan’s Quintet in Higdon & et al. (2008; Boquien et al. 2009; Higdon et al. 2010; Cluver et al. 2010) and Arp 105 in Higdon & et al. (2008; Boquien et al. 2009; Higdon et al. 2010). The MIPS (Rieke et al. 2004) observations are presented here for Arp 102 and NGC 5291 (also presented in Higdon et al. 2010, Boquien et al. 2010). The remainder were presented in Smith et al. (2007a).

The IRAC data were processed using the IRAC pipeline. To be considered a ISFO a source must satisfy the following criteria: (1) it must coincide with a tidal feature, either in the optical or HI, (2) it must be point like in the 8  $\mu\text{m}$  images, with at least 6 contiguous pixels  $\geq 3\sigma$  relative to the sky background, and (3) it must be detected to  $\geq 3\sigma$  in both the 3.6  $\mu\text{m}$  and 8  $\mu\text{m}$  bands using aperture photometry.

To estimate the likelihood that our ISFO candidates are unrelated background sources we multiply their corresponding 8 $\mu\text{m}$  source surface densities (Fazio et al. 2004a) times the surface area of the plume or tail they are found in. For example, the four ISFO candidates in the northern plume of Arp 65 have 8  $\mu\text{m}$  magnitudes from 14.02 to 13.85, with an average of 13.94. From the 8  $\mu\text{m}$  source counts in Fazio et al. (2004a) we would expect a surface density of 0.13 arcmin<sup>-2</sup> for objects in this magnitude range. The northern plume covers 0.13 arcmin<sup>2</sup>, which gives a less than 2% probability that one of the four is an unrelated background source. We derive similar estimates for our other ISFOs, except for Arp 102, where because of the relative faintness of the ISFOs we estimate a 20% probability that one of the two candidates is unrelated. Interestingly enough, one of these (Arp 102-N2) appears to be a background elliptical (or possibly an old stellar cluster) based on its declining 3.6  $\mu\text{m}$  through 8  $\mu\text{m}$  spectral energy distribution (SED, see Table 2).

Flux densities and limits were derived using circular apertures. We adopt the zero-point flux densities in the four IRAC bands as given in Reach et al. (2005), i.e., 280.9 $\pm$ 4.1, 179.7 $\pm$ 2.6, 115.0 $\pm$ 1.7, and 64.13 $\pm$ 0.94 Jy at 3.6, 4.5, 5.8, and 8.0  $\mu\text{m}$ , respectively. For most sources the aperture radii are either 3'' or 5'', with background measurements derived from annuli with inner/outer radii of 3'' – 7'' or 5'' – 10'' respectively. A small subset of sources (e.g., Arp 105-N1) were more extended (though still core dominated) and required larger sized apertures. Aperture corrections were applied using the recommended values in the Spitzer Observers Manual (SOM)<sup>1</sup>. Measured positions are listed in Table 1, while flux densities and 1 $\sigma$  uncertainties for 67 ISFOs along with the object and sky aperture sizes used are listed in Table 2. For non-detections we calculate upper-limits (3 $\sigma$ ) defined as  $3\sigma\sqrt{N}$ , where  $\sigma$  and  $N$  are the *rms* and number of pixels in the source aperture respectively. These are also listed in Table 2. It is worth noting that in Stephan’s Quintet there are six objects

---

<sup>1</sup><http://ssc.spitzer.caltech.edu/documents/som/>

detected in  $^{12}\text{CO}(J=1-0)$  by Petitpas & Taylor (2005) that are not detected at  $8\ \mu\text{m}$ .

Preliminary data processing and calibration were performed on the MIPS  $24\ \mu\text{m}$  data using the standard pipeline, producing a set of basic calibrated data products. The data were further processed using the MOPEX software package (version 18.2.2; Makovoz & Marleau 2005). This consisted of deleting the defective first frames in each scan, recalculating flat-fields and background levels, and re-mosaicing each field. The diffraction limited resolution at  $24\ \mu\text{m}$  is  $5.7''$ , and a few targets are sufficiently bright to show faint Airy diffraction rings (see Table 2). The  $1\sigma$  sensitivities vary from one target field to another, but are typically  $\sim 0.1\ \text{MJy sr}^{-1}$ . We adopt a zero-point flux density of  $7.14\ \text{Jy}$  at  $24\ \mu\text{m}$ , though it should be noted that this value is uncertain at the  $\pm 5\%$  level (see Engelbracht et al. 2007 for a discussion of this and other calibration issues).  $24\ \mu\text{m}$  flux densities (or  $3\sigma$  limits) were derived for each ISFO candidate using circular apertures of radii  $6''$  or  $13''$ , depending on the source brightness and degree of isolation. Local sky emission was measured within annuli with inner/outer radii of  $20''$  and  $32''$ . These are also listed in Table 2. Point-source aperture corrections have been applied using the recommended values in the MIPS Users Guide.  $3\sigma$  upper-limits are calculated for non-detections with  $3\sigma\sqrt{N}$  as with IRAC. As a check of our photometry we derived flux densities using the point-source fitting algorithm APEX in the MOPEX photometry package and found very good agreement (i.e., within the quoted  $1\sigma$  uncertainties). In this work we will quote the flux densities obtained using circular aperture photometry to be consistent with the IRAC data, for which point-source fitting is not recommended.

### 3.2. Spitzer Spectroscopy

In this paper we present Spitzer spectra of ten ISFOs (see Tables 3-5). The IRS low resolution spectra (IRS-LORES) were obtained with the Short-Low module (IRS-SL), which operates between  $5.2$  and  $7.7\ \mu\text{m}$  (IRS-SL2) and  $7.4$  and  $14.5\ \mu\text{m}$  (IRS-SL1) and the IRS Long-Low module (IRS-LL), which operates between  $14$  and  $21.3\ \mu\text{m}$  (IRS-LL2) and  $19.5$  and  $36.0\ \mu\text{m}$  (IRS-LL1). IRS-SL and IRS-LL have a resolving power,  $R = \frac{\lambda}{\Delta\lambda} \sim 60\text{-}130$ . The high resolution data (IRS-HIRES) were obtained using the IRS Short-High module (IRS-SH), which encompasses the range  $9.9 - 19.6\ \mu\text{m}$ , and the IRS Long-High module (IRS-LH), which spans  $18.7 - 37.2\ \mu\text{m}$ . IRS-HIRES has a resolving power,  $R = \frac{\lambda}{\Delta\lambda} \sim 600$ .

Observations were made in the IRS Staring Mode AOR with a high accuracy blue peak-up using a star from the Two Micron All Sky Survey catalog (Cutri et al. 2003). We obtained a series of  $4 \times 60\ \text{s}$  exposures in each of the two IRS-SL bands, and  $4 \times 120\ \text{s}$  exposures in the two IRS-LL bands. The IRS HIRES data was obtained with  $3 \times 120\ \text{s}$  and  $14 \times$

60 s for IRS SH and IRS LH respectively. The Staring Mode AOR splits the integration time between two nominal nod positions on each slit. Only Arp 87-N1 was observed in all the IRS apertures. Some of the data obtained as part of the SAINTS program is not presented here as it was either of too low signal to noise to be useful, or the slit orientation resulted in data where emission from the ISFO was blended with the parent galaxy. IRS-SL spectra were obtained for Arp 72-S1, Arp 82-N1, Arp 84-N1 Arp 87-N1 (Higdon et al. 2010), “Ambartsumian’s knot” (Arp 105-S2, Higdon & Higdon 2008; Boquien et al. 2009; Higdon & Higdon 2010), Arp242-N3 in the Mice (Higdon et al. 2010), Arp284-SW, SQ-A in Stephan’s Quintet (Higdon & Higdon 2008; Higdon et al. 2010), and TDG N and TDG S in NGC 5291 (HHM06). There are IRS-LL spectra for Arp 72-S1 and Arp 82-N1, and no HIRES observations of Arp 105-S2 and Arp 242-N3.

The spectral data were processed as far as the un-flat-fielded two dimensional image using the standard IRS S18.5 pipeline (see the SOM for further observing mode and pipeline details). Due to the crowding of the Spitzer focal plane the individual IRS apertures are not aligned, e.g., SH is orientated  $\sim 85^\circ$  with respect to LH. Depending on the orientation on the sky the slit may contain emission from more than one ISFO and/or the parent galaxy. The spectra were extracted and sky subtracted manually using the Spectroscopy Modeling Analysis and Reduction Tool (SMART, Higdon et al. 2004) software to ensure that the extracted spectra were dominated by light from a single ISFO and that the sky spectrum was representative of the background emission.

The IRS-LORES sky data is acquired serendipitously during the standard observation. For example, SL1 and SL2 are one long slit, so when the source position is nodded between two positions in SL1, data is also acquired simultaneously in SL2 which is pointing off source. Combining the SL1 and SL2 observations offers the potential for a SL1-sky spectrum selected in either the region of the slit adjacent to the source during the SL1 observation (nod-data) or from a region in one of the two off-source SL1 spectra acquired during the SL2 on-source nod-observation. To maximize the signal-to-noise all data was inspected manually using SMART. The data from each nod for each slit were collapsed in the cross-dispersion direction to determine manually which data should be co-added to define the sky. The sky data so defined are then coadded and subtracted from the two dimensional coadded source data. The sky-subbed IRS-LORES two-dimensional data was then collapsed in the cross-dispersion direction to determine the position of the ISFO in the slit and to check for blending with other objects. A column was extracted, whose width in the cross-dispersion direction scales with the instrument point spread function (see the SOM, Higdon et al. 2004, and HHM06 for further details). A full aperture extraction was applied to the HIRES data which included dedicated off-source sky observations.



The extracted ISFO spectra were flat-fielded and flux-calibrated by extracting and sky subtracting un-flat-fielded observations of the calibration stars HR 7341 (IRS-SL/LL) and  $\xi$  Dra (IRS-SH/LH), which are subsequently divided by the corresponding template (Decin et al. 2004, Cohen et al. 2003) to generate a one-dimensional relative spectral response function (RSRF). The RSRF was then applied to the ISFO spectra to produce flux-calibrated spectra. The final step of stitching spectral orders together was accomplished in the following manner: the data from each IRS module is sky subtracted. Using the photometry routines in SMART the SL spectra are scaled to match the IRAC 8  $\mu$ m photometry. If MIPS 24  $\mu$ m photometry is available the LL and LH spectra are scaled to match the value reported in Table 2. If there is no 24  $\mu$ m photometry the spectra are stitched to the 8  $\mu$ m-scaled SL spectra using the overlapping continuum regions. For example, for the observation of the ISFO in Arp 72 the LL slit was orientated along the tidal tail, the SL data was scaled by 1.69, LL by 0.76, SH by 4.0 and LH by 0.63. As a check on this calibration method we looked at the flux ratio of the brightest lines observed in Arp 72-S1. The ratio of the high resolution line fluxes to low resolution, was  $R([\text{Ne III}] 15.56 \mu\text{m}) = 0.89$ ,  $R([\text{S III}] 18.71 \mu\text{m}) = 1.03$  and  $R([\text{S IV}] 10.51 \mu\text{m}) = 1.00$ . The aperture scale factors are listed in Table 3.

Figure 2 shows the IRS low resolution spectra. The data are plotted in each object’s rest-frame. The broad emission features from PAHs at 6.2, 7.7, 8.6, 11.3, and 12.6  $\mu$ m are clearly present. Some of the spectra show emission from  $[\text{S IV}] 10.51 \mu\text{m}$  as well as 0-0 S(3) 9.67  $\mu$ m and 0-0 S(1) 17.04  $\mu$ m lines from molecular hydrogen. Emission from  $[\text{Ne II}] 12.81 \mu\text{m}$  is blended with the PAH feature, but the line is distinct in the IRS-HIRES observations. Figure 3 shows the line profiles from the IRS-HIRES observations. The line strengths are measured using SMART and are listed in Table 4. The strengths of the PAH features are measured using PAHFIT (Smith et al. 2007b) and are listed in Table 5. For Arp 72-S1 and Arp 82-N1 we have scaled LL spectra, which are included in the PAHFIT. The results do not change when only the SL data is fitted. For consistency between the data sets for the ISFOs reported here we scale the NGC 5291-S spectrum to match the IRAC 8  $\mu$ m photometry (the NGC 5291 N spectrum matches the photometry), and fit the PAHs in both NGC 5291 N and NGC 5291 S spectra using PAHFIT. Apart from the 11.3  $\mu$ m to 7.7  $\mu$ m PAH ratio for NGC 5291-S, the PAH ratios are within 20% of those reported in HHM06.

Extinction due to silicate absorption is best constrained for Arp 72-S1 and Arp 82-N1 where the low resolution spectral coverage includes the two silicate features, the Si-O stretching mode at 9.7  $\mu$ m and O-Si-O bending mode at 18  $\mu$ m. The fits show no evidence for absorption. The majority of our sample are limited to the scaled SL observations where it is difficult to discriminate between silicate absorption at 9.7  $\mu$ m and PAH emission on either side of the silicate feature. For the analysis in this paper we assume all targets have minimal line-of-sight silicate extinction ( $A_v \leq 3$  mag). This is also consistent with the results

for the Spitzer Infrared Nearby Galaxies Survey (SINGS, Kennicutt et al. 2003) where 5 - 38  $\mu\text{m}$  spectra were available. In that sample only 8 of the 59 galaxies had measureable extinction at 9.7  $\mu\text{m}$  (Smith et al. 2007b).

## 4. RESULTS AND DISCUSSION

### 4.1. Characterizing The PAHs

The 5-38  $\mu\text{m}$  SL spectra are dominated by broad emission features. These features are generally attributed to the spontaneous emission of an infrared photon from PAHs that have been vibrationally excited following a single optical/UV photon absorption. The resulting emission spectrum depends on the heat capacity (size) of the PAH, and is largely independent of the starlight intensity. For example, the models by Li & Draine (2001) assume the carbonaceous grains have PAH-like properties when the grains have  $\leq 10^3$  carbon atoms, corresponding to a size of  $\sim 10\text{\AA}$ , and graphitic properties when much larger ( $\geq 100\text{\AA}$ ). Emission from the larger grains will peak at much longer wavelengths than observed with the IRS. The PAH spectrum may also depend on the overall structure of the PAH, i.e., linear vs. concentrated (Bakes et al. 2001).

PAHs have a low ionization potential (6-7 eV) and can be easily ionized through photoelectric emission ( $\text{PAH}^+$ ) and electron capture ( $\text{PAH}^-$ ) (Allamandola et al. 1985). The grain charging is dependent on the gas temperature, electron density, the ultraviolet radiation field, and the cross-sections for PAH electron capture and photoelectric emission (Draine & Li 2007, Weingartner & Draine 2001).

The 11.3  $\mu\text{m}$  feature is a vibrational C-H out of plane bending mode from “solo” CH groups implying large PAHs. The 6.2 and 7.7  $\mu\text{m}$  features are from a C-C stretching mode. Unlike the 11.3  $\mu\text{m}$  PAH, the 7.7  $\mu\text{m}$  feature has a much larger absorption cross-section in  $\text{PAH}^+$  ions than neutral PAHs (see Figure 3 in Draine & Li 2007) i.e., the relative band strength of the  $\text{PAH}_{11.3\mu\text{m}}/\text{PAH}_{7.7\mu\text{m}}$  ratio (hereafter,  $R_{11/7}$ ) is large for neutral PAHs and decreases by an order of magnitude for ionized PAHs (Draine & Li 2001, see Figure 16 and references therein). In an empirical study of Galactic star forming regions Galliano et al. (2008) concluded that the main driver of  $R_{11/7}$  is the PAH ionization fraction. These differences in the relative PAH band strengths are driven by the relative ionization to recombination rates, which is a function of the ratio of intensity of the stellar radiation field to the electron density. Other factors that affect the  $R_{11/7}$  ratio to a lesser extent are the PAH size, the extinction, and the hardness of the ISRF (Draine & Li 2001, Galliano et al. 2008).

Figure 4 displays the  $\text{PAH}_{6.2\mu\text{m}}/\text{PAH}_{7.7\mu\text{m}}$  ratio ( $R_{6/7}$ ) versus  $R_{11/7}$  for 9 ISFOs. For

comparison we selected sources in the literature which have a signal-to-noise ratio  $\geq 3$  for each PAH band. The PAH flux was measured using PAHFIT (Smith et al. 2007b). We include results from SINGS, which is a comprehensive set of observations of the inner 1-10 kpc<sup>2</sup> of 75 nearby normal galaxies (Kennicutt et al. 2003). Each galaxy is identified as having either a HII-like or weak AGN-like nucleus. Figure 4 also shows 24 HII-like and 24 AGN-like SINGS galaxies (Smith et al. 2007b), 6 BCDs (Hunt et al. 2010), an additional 6 BCDs, 16 starburst galaxies, 27 sources within three local giant HII regions: NGC 3603 in the Milky Way, 30 Dor. in the LMC, and N 66 in the SMC (Lebouteiller et al. 2011 and references therein).

Two thirds of the ISFO sample have an  $R_{6/7}$  similar to the SINGS and starburst galaxies. The SINGS-AGN sources tend to have a smaller ratio. Theoretical models show that  $R_{6/7}$  increases as the PAHs get smaller (Draine & Li 2001). In general terms the PAH size distribution is weighted toward a population with large PAHs in sources with a weak AGN, medium sized in the SINGS-HII and starburst galaxies, and smallest in the BCDs and in the three local giant HII regions (NGC 3603, 30 Dor. and N 66). In Arp 105-S2, Arp 82-N1 and Arp 284-SW1 the relative strengths of the PAH 6.2 and 7.7  $\mu\text{m}$  emission are similar to what is observed in BCDs and local giant HII regions corresponding to the models with bright emission from small PAHs, with the number of carbon atoms,  $N_C \leq 50$ , as opposed to a model with bright emission from larger PAHs with  $N_C \sim 100$ , which is appropriate for the other ISFOs and the SINGS-HII and starburst galaxies (see Figure 16 in Draine & Li 2001).

The ISFO  $R_{11/7}$  ratios are consistent with the range seen in the SINGS AGN and HII sources and starburst galaxies, and some of the NGC 3603 regions in the Milky Way. The ISFO  $R_{11/7}$  is lower than what is observed in the regions in 30 Dor. and N 66 and many of the BCDs. Again comparing the data to the Draine & Li (2001) models the ISFOs are consistent with a mixed charge distribution with a large fraction of the PAHs being neutral ( $\geq 50\%$ ) in order to produce the observed bright 11.3  $\mu\text{m}$  PAH emission.  $R_{11/7}$  for the local giant HII regions is consistent with a mostly neutral PAH population. The ISFO  $R_{11/7}$  and  $R_{6/7}$  (except  $R_{6/7}$  for three ISFOs) values are comparable to the global properties of spirals and starburst galaxies rather than BCDs and sources in three local giant HII regions.

## 4.2. ISRF Hardness and Young Stellar Population

Both the neon and the sulfur line flux ratios can be used to constrain the properties of the underlying starburst. The  $[\text{S IV}]/[\text{S III}]$  and  $[\text{Ne III}]/[\text{Ne II}]$  line flux ratios give a measure of the hardness of the ISRF, which depends on the effective temperature of the ionizing stars

and the ionization parameter. Lowering the metallicity produces hotter main sequence stars for a given mass, and the radiation is harder due to reduced line blanketing and blocking. Verma et al. (2003) used the  $[\text{S IV}]/[\text{S III}]$  and  $[\text{Ne III}]/[\text{Ne II}]$  line flux ratios as an excitation diagnostic for a sample of starburst and BCD galaxies. Their data is reproduced in Figure 5 along with our results for the ISFOs, a sample of BCDs from Hunt et al. (2010), clumps in the ring galaxy Arp 143 (Beiraro et al. 2009) and a sample of 27 sources in three local giant HII regions in NGC 3603, 30 Dor., and N 66 (Lebouteillier et al. 2011). The ISFOs form a group between the starburst galaxies in the bottom left quadrant of the plot, and the BCDs in the upper right quadrant. The line flux ratios indicate moderate excitation consistent with our results for NGC 5291 N and NGC 5291 S (HHM06), and with the interacting galaxy pairs NGC 4038/NGC 4039 and NGC 3690B/C (Verma et al. 2003), the BCDs Haro 3 and Mrk 996 (Hunt et al. 2010) and regions in NGC 3603 and 30 Dor. Arp 84-N1 has a lower neon ratio consistent with the starburst galaxies.

Hunt et al. (2010) observed an increase in the  $[\text{Ne III}]/[\text{Ne II}]$  flux ratio with decreasing oxygen abundance. The BCDs tend to have larger neon ratios and the starburst sample tend to have lower values. The sources in the giant HII regions mostly have neon line flux ratios greater than one. Both Madden et al. (2006) and Lebouteillier et al (2011) argue that PAHs are destroyed in harsh radiation fields with  $[\text{Ne III}]/[\text{Ne II}] \gtrsim 2-3$ . The ISFOs have neon line flux ratios similar to those observed in the regions in NGC 3603 (solar metallicity). The ISFO neon and sulfur line flux ratios are lower than the observed ratios in the sources in N 66 ( $0.2 Z_{\odot}$ ) and the majority of sources in 30 Dor. ( $0.6 Z_{\odot}$ ). The individual sources in NGC 3603, 30 Dor. and N 66 exhibit a spread in the line flux ratios for a given abundance as they sample different parts of the giant HII regions. Only three ISFOs from our sample of nine with neon line flux data have abundance estimates (see Section 2) and the average neon line flux ratio is 1.3. If one-third to solar metallicity or higher is typical for the ISFOs, then the ISFOs fill the gap in the distribution of the global neon line flux as a function of metallicity, forming a group between the starburst and BCD galaxies.

An upper limit to the age of the most recent episode of star formation can be estimated by comparing the observed  $[\text{Ne III}]/[\text{Ne II}]$  line flux ratio to values generated for a range of population synthesis models (e.g., Thornley et al. 2000, Madden et al. 2006). Assuming the metallicity is  $\sim 0.2-1 Z_{\odot}$  and that the star formation occurred in a single burst gives an upper limit of 6 Myr, i.e., recent star formation in the ISFOs.

In Figure 6 we plot  $R_{11/7}$  as a function of the  $[\text{Ne III}]/[\text{Ne II}]$  line flux ratio. Hunt et al. (2010) observed an increase in  $R_{11/7}$  in BCDs with neon ratios greater than one. The  $7.7 \mu\text{m}$  PAH emission arises from a fairly broad range of grain size (Schutte et al. 1993). Hunt et al (2010) propose that a hard intense ISRF may destroy the small grains which contribute

to the  $7.7\ \mu\text{m}$  PAH emission whilst not impacting on the intensity of the  $11.3\ \mu\text{m}$  emission. If the neon line flux ratio is a good proxy for the hardness of the ISRF in the ultraviolet, the observed scatter in  $R_{11/7}$  for objects with  $[\text{Ne III}]/[\text{Ne II}] > 1$  suggest that the hardness of the ISRF, as measured by the infrared line flux ratios, is not the main driver of  $R_{11/7}$ . For example, there is no significant increase in  $R_{11/7}$  in the six ISFOs with  $[\text{Ne III}]/[\text{Ne II}] > 1$  and in one case for a BCD when  $[\text{Ne III}]/[\text{Ne II}] > 10$ . Similarly, moderately high  $R_{11/7}$  values are observed in two SINGS-AGN galaxies and three sources in the local Giant HII regions which have  $[\text{Ne III}]/[\text{Ne II}] < 1$ . Small PAHs need not be destroyed. The  $7.7\ \mu\text{m}$  emission is stronger in ionized PAHs as compared to neutral PAHs, if the PAHs tend to be neutral in the three local giant HII regions and in BCDs, then the difference in the PAH ion fraction in these sources, as compared to ISFOs and SINGS galaxies, could be driving the  $R_{11/7}$ .

Figure 7 shows the PAH  $8.6\ \mu\text{m}/7.7\ \mu\text{m}$  ratio (hereafter  $R_{8/7}$ ) as a function of the  $[\text{Ne III}]/[\text{Ne II}]$  line flux ratio. The PAH  $8.6\ \mu\text{m}$  emission is from large PAHs with a minimum of 100 carbon atoms (Bauschlicher 2008) whereas the  $7.7\ \mu\text{m}$  PAH emission is from a mixture of small and large PAHs. Both features have larger capture cross-sections for  $\text{PAH}^+$  ions than for neutral PAHs. There is a large scatter in  $R_{8/7}$  for each source type, and especially when  $[\text{Ne III}]/[\text{Ne II}] \gtrsim 1$ .  $\langle R_{8/7} \rangle = 0.20 \pm 0.05$  for 8 ISFOs which is consistent with the ratio of  $\langle R_{8/7} \rangle = 0.17 \pm 0.03$  for 45 SINGS galaxies.  $\langle R_{8/7} \rangle = 0.45 \pm 0.33$  for 19 sources in the three local giant HII regions ( $\langle R_{8/7} \rangle = 0.36 \pm 0.12$  for 13 sources in 30 Dor.), and  $\langle R_{8/7} \rangle = 0.31 \pm 0.13$  for 8 BCDs (this does not include Mrk 1315 with  $R_{8/7} = 1.8$ ).

The ionization balance depends on the gas temperature, electron density and ultraviolet radiation field (Weingartner & Draine 2001). The PAH ion fraction can drive the relative strengths of the PAH bands. As the PAH ion fraction increase and/or the fraction of large PAHs increases the PAHs can absorb longer wavelength photons and the observed emission is less dependent on the hardness of the radiation field. The relative PAH band strengths in the ISFOs are consistent with a mixed population of grain sizes that contain a much larger fraction of PAH ions compared to PAHs in BCDs and sources in local giant HII regions.

### 4.3. Warm Molecular Gas

Warm molecular gas is detected in 7 of 8 (88%) of the ISFOs observed with IRS-HIRES (see Table 4). To derive the mass of warm molecular hydrogen we assume that the emission is optically thin. The critical densities of the low J levels are relatively low ( $n_{\text{cr}} < 10^3\ \text{cm}^{-3}$ ) and we assume that the populations are in LTE. Adopting an ortho to para ratio of 3 we construct excitation diagrams (see HHM06 for further details). The excitation temperature is the reciprocal of the slope of the linear fit to the natural logarithm of the

number of molecules divided by the statistical weight in the upper level of each transition versus the upper level of each transition. The mass is derived using the calculated excitation temperature and the highest signal-to-noise line, the IRS-HIRES 0-0 S(1) 17.03  $\mu\text{m}$  line. Both the stitching together of the individual spectra (Section 3.2) and the use of a single temperature component model add uncertainty to the derived molecular mass.

For Arp 72-S1 we constructed an excitation diagram using the IRS-HIRES S1 line along with the IRS-LORES 0-0 S(0) and 0-0 S(2) lines. For a single component model the excitation temperature is  $T_{ex} = 210 \pm 9$  K with  $\sim 10^6 M_\odot$  of warm  $\text{H}_2$ . For Arp 82-N1 we combined the IRS-HIRES detections of the 0-0 S(0) and 0-0 S(1) lines with the IRS-LORES measurements of the 0-0 S(2) and 0-0 S(3) lines. The excitation temperature is  $T_{ex} = 214 \pm 6$  K with  $\sim 10^6 M_\odot$  of  $\text{H}_2$ .

In Arp87-N1, Arp284-SW and SQ-A we only detect the 0-0 S(1) line. Adopting a value of  $T_{ex} = 200$  K we estimate that there is  $\sim 10^6 M_\odot$  of warm  $\text{H}_2$  in Arp 87-N1 and Arp 284-SW1 and  $\sim 10^7 M_\odot$  of  $\text{H}_2$  in SQ-A. These results are similar to those derived for NGC 5291 N and NGC 5291 S (HHM06, note a higher excitation temperature of  $\sim 400$  K was estimated with a fit limited to the 0-0 S(1) and 0-0 S(2) lines. Lowering the excitation temperature gives a higher gas mass).

ALMA and CARMA observations are needed to constrain the cold molecular gas mass and derive the warm gas fraction. Based on the limited observations of ISFOs (HHM06 reported that the warm gas mass in NGC 5291-N and NGC 5291-S is less than 1% of the cold gas mass inferred from  $^{12}\text{CO}$  (1-0) observations of Braine et al. 2001) we expect it to be  $< 1\%$ , which is similar to the warm gas fraction in a sample of 59 ULIRGs (Higdon et al 2006a). These two very different classes of objects have warm  $\text{H}_2$  excitation temperatures and masses consistent with emission from gas in PDRs.

## 4.4. Characterizing the Mid-infrared Spectral Energy Distribution

### 4.4.1. Spitzer Broadband Colors

In Figure 8 we show four Spitzer two-color diagrams for our sample of 67 ISFOs. For comparison the SINGS sample (Dale et al 2005), a sample of star forming dwarf galaxies collated from the literature (Smith & Hancock 2009 and references therein), a sample of clumps identified in the disks of interacting galaxies collated from the literature (Arp 24, Arp 82, Arp 244, Arp 284 and Arp 285; Lapham et al. 2013 and references therein) and some template colors of HII regions, planetary nebulae (PNe), and supernovae remnants (SNRs) in M 33 (Verley et al. 2007) are included. It should be noted that the individual sources

used to form each of the M 33 templates exhibit a wide range of Spitzer colors (for example, see the middle panel of Figure 12 in Verley et al. 2007).

In general, the ISFOs have Spitzer colors similar to star forming clumps in the disks of interacting galaxies. However, the ISFOs are redder on average in  $[4.5] - [8.0]$  colors than the integrated colors of the SINGS galaxies or star forming dwarfs. This is likely a consequence of bright PAH emission in the  $8 \mu\text{m}$  band, as observed in the ISFO spectra displayed in Figure 2.

This difference is apparent in panel (A) of Figure 8, where the ISFOs lie in two zones. A red population with  $[4.5] - [8.0] > 3$  encompasses 70% of the ISFOs (47/67). Half of these (one third of the whole sample) have  $[4.5] - [8.0] > 3.7$ . These are redder than the global colors of the majority of the comparison galaxies, most likely due to enhanced non-stellar emission, particularly PAHs in the  $8 \mu\text{m}$  band. The remaining third, which include the ISFOs in Arp 242, are blue in this color, similar to the median value of the SINGS galaxies. These may be more quiescent star forming regions, as they tend to be bluer in the other Spitzer colors as well.

ISFOs have a  $[3.6] - [4.5]$  color similar to that of star forming clumps in the disks of interacting galaxies, as well as the global colors of spirals and dwarfs (panels A and B of Figure 8). A  $[3.6] - [4.5]$  color close to zero is expected if the emission in both bands is predominantly starlight.

As shown in panels (B)-(D) in Figure 8, the ISFOs have  $[3.6] - [24.0]$  colors similar to those of the interacting disk star forming knots, SINGS-HII, dwarf galaxies and half of the SINGS-AGN galaxies. Some of the dwarfs, star forming clumps in interacting galaxies, and one ISFO (Arp 82-N1) are redder in this color than the SINGS galaxies, which could be caused by intense star formation boosting the  $24 \mu\text{m}$  dust emission relative to the starlight.

The colors of ISFOs and the star forming clumps in interacting galaxy disks are clearly separated from dwarfs when the  $[3.6] - [24.0]$  color is plotted as a function of either the  $[3.6] - [8.0]$  (panel (D) in Figure 8) or  $[8.0] - [24.0]$  colors (panel (C) in Figure 8), but not the  $[3.6] - [4.5]$  color (panel (B) in Figure 8). For a given  $[3.6] - [24.0]$  color the ISFOs tend to be redder in  $[3.6] - [8.0]$  than the dwarfs. Likewise for a given  $[3.6] - [24.0]$  color the ISFOs are bluer in  $[8.0] - [24.0]$  than the dwarfs. These color offsets are consistent with our spectroscopic results that show the ISFOs to have bright PAH emission. In contrast, results in the literature show that low metallicity dwarfs have intense UV fields and weak PAH features in the  $8 \mu\text{m}$  band, while the  $24 \mu\text{m}$  emission arises primarily from larger dust grains. A search for the reddest ISFOs and star forming clumps in the disks of interacting galaxies can be made using the criteria  $[4.5] - [8.0] > 3.7$ .

#### 4.4.2. Fraction of Dust Luminosity From PDRs

The ISFOs were selected based on their bright 8  $\mu\text{m}$  emission. Some example 3.6 - 24  $\mu\text{m}$  SEDs are shown in Figure 9. The majority of the ISFOs have a distinctive ‘notched-shaped’ SED, i.e., the flux falls from 3.6 to 4.5  $\mu\text{m}$ , and then steeply rises from 4.5 to 8.0  $\mu\text{m}$ . This spectral shape is characteristic of star forming regions illuminated by an intense stellar field, and was observed in the ISFOs in NGC 5291 (HHM06). Some of the SEDs have a flux that decreases from 3.6  $\mu\text{m}$  through 5.8  $\mu\text{m}$  before rising. In one case, Arp 102-N2, the SED slopes downward from 3.6  $\mu\text{m}$  through 24  $\mu\text{m}$ , which is characteristic of evolved stellar populations, i.e., an elliptical galaxy. This may be a ISFO devoid of gas and dust or more likely, an object not associated with Arp 102.

Draine et al. (2007) fit physical dust models (see Draine & Li 2007) to 65 SINGS galaxies using IRAC, MIPS and in some cases sub-mm photometry. The IR/sub-mm emission from the dust depends not only on the amount of dust, but also on the location. Draine et al. (2007) conclude that a large fraction of the dust mass in the SINGS galaxies is in the diffuse ISM. This diffuse ISM can be characterized with an ISRF with an approximately constant intensity,  $U_{\text{min}} = \alpha U$ , where  $\alpha$  is a scale factor  $\leq 10$ ,  $U = 0.88 G_{o,dens}$ , where  $G_{o,dens}$  is the ratio of the 6-13.6 eV energy density relative to the value of  $5.29 \times 10^{-14} \text{ erg cm}^{-3}$  measured by Habing (1968) for the local ISRF.

Most of the dust mass in galaxies is relatively cool and radiates longward of 60  $\mu\text{m}$ . A small fraction of the total dust mass resides in regions illuminated by a more intense radiation field ( $U > U_{\text{min}}$ ), for example PAHs in PDRs. In one in seven SINGS galaxies the emission from these intensely illuminated regions (likely PDRs) contribute a significant fraction ( $\gtrsim 30\%$ ) of the total power emitted by the dust grains (Draine et al. 2007).

Our dataset is limited to photometry at wavelengths  $< 30 \mu\text{m}$  and is insufficient to be used to fit models, and to derive the dust mass and properties in detail. However we can use the Draine & Li (2007) models, and the Draine et al. (2007) results for the SINGS galaxies, to estimate what fraction of the dust luminosity is likely to come from intensely illuminated ( $U > 10^2$ ) regions (e.g., PDRs  $f_{\text{Intense}}$ ), and where the bulk of the IR emission originates in the ISFOs.

Emission from dust (including PAHs) in the ISM heated by a diffuse ISRF, has  $\lambda F_{\lambda}(8\mu\text{m}) > \lambda F_{\lambda}(24\mu\text{m})$  (Draine & Li 2007). In regions illuminated by intense starlight the emission at 24  $\mu\text{m}$  is from both single-photon heating of PAHs and multi-photon heating of larger grains. Emission from these more intensely illuminated regions, i.e., PDRs, has  $\lambda F_{\lambda}(8\mu\text{m}) \leq \lambda F_{\lambda}(24\mu\text{m})$ .

Following the recipe in Draine & Li (2007) we will assume that the flux measured in the



IRAC 3.6  $\mu\text{m}$  band apertures is stellar in origin, and can be approximated by emission from a 5000 K blackbody. We extrapolate this stellar contribution to 8  $\mu\text{m}$  and 24  $\mu\text{m}$  in order to calculate the non-stellar flux in these bands using  $F_{\nu(NS)}(8 \mu\text{m}) = F_{\nu}(8 \mu\text{m}) - 0.260 F_{\nu}(3.6 \mu\text{m})$  and  $F_{\nu(NS)}(24 \mu\text{m}) = F_{\nu}(24 \mu\text{m}) - 0.0326 F_{\nu}(3.6 \mu\text{m})$ . In the absence of extinction and the presence of red giants and AGB stars this simple blackbody subtraction will overestimate the non-stellar (dust) emission. In the presence of bright 3.3  $\mu\text{m}$  PAH emission the stellar emission will be over-estimated. The 3.3  $\mu\text{m}$  PAH emission in the 3.6  $\mu\text{m}$  band is sensitive to the abundance of the smallest PAHs and the PAH charge state (Draine & Li 2007).

The non-stellar emission in the 8  $\mu\text{m}$  band is dominated by single photon heating of PAHs, and it is proportional to total starlight power absorbed by the dust (i.e.,  $\nu F_{\nu}(71\mu\text{m}) + \nu F_{\nu}(160\mu\text{m})$  flux; Draine & Li 2007). Using the photometry for 23 SINGS-HII spiral galaxies (Dale et al. 2007) we find  $\langle \nu F_{\nu}(71\mu\text{m}) + \nu F_{\nu}(160\mu\text{m}) \rangle = (5.00^{+1.5}) \times \langle \nu F_{\nu NS}(8\mu\text{m}) \rangle$ .

Draine & Li (2007) show that the fraction of the total emission supplied from high intensity (likely PDR) regions with  $U > 10^2$  is related to the observed non-stellar power at 24  $\mu\text{m}$  and 8  $\mu\text{m}$ .

$$P_{24} - 0.14P_8 = \frac{\langle \nu F_{\nu NS}(24\mu\text{m}) \rangle - 0.14 \langle \nu F_{\nu NS}(8\mu\text{m}) \rangle}{\langle \nu F_{\nu}(71\mu\text{m}) \rangle + \langle \nu F_{\nu}(160\mu\text{m}) \rangle} \quad (1)$$

The numerator in Equation (1) is a measure of the emission from large grains that will only radiate at 24  $\mu\text{m}$  when exposed to intense starlight. The 24  $\mu\text{m}$  emission from single-photon heating is subtracted using the weighted 8  $\mu\text{m}$  flux, as the 8  $\mu\text{m}$  emission is dominated by single-photon heating of PAHs.  $f_{Intense}$  for the SINGS galaxies is given by the following relation (see Figure 24, Draine et al. 2007):

$$f(Intense; L_d; U > 10^2) \sim 1.05(P_{24} - 0.14P_8 - 0.035)^{0.75} \quad (2)$$

The ISFOs and SINGS-HII galaxies have similar [8.0] - [24.0] colors, and we assume the ISFOs follow this relation. The ISFOs were not observed with MIPS in the 71  $\mu\text{m}$  and 160  $\mu\text{m}$  bands. However by substituting  $(5.00^{+1.5}) \times \langle \nu F_{\nu NS}(8\mu\text{m}) \rangle$  for the denominator in Equation (1) we can estimate  $f_{Intense}$  using Equation (2). The largest uncertainty is the assumption that the PAH abundance in the ISFOs is similar to that observed in the SINGS sample. We do not know of any objects with an enhanced PAH abundance relative to SINGS-HII, but a PAH deficit is observed in AGN environments and low metallicity systems. The ISFOs in our spectral sample with published metallicities have values of one third solar or higher, this is above the regime where dwarfs are observed with a PAH deficit (e.g., Madden et al. 2006), and the ISFOs have bright PAH emission. If the other ISFOs

in the photometric sample have a lower abundance and a corresponding PAH deficit, we will underestimate the total starlight power absorbed by the dust using this method, and overestimate  $f_{Intense}$ . However, we do not expect there to be a PAH deficit, the ISFO spectra have bright  $8\mu\text{m}$  features, and the larger photometric sample have a ‘notched-shaped’ SED characteristic of star forming regions with bright PAH emission.

Some example ISFO SEDs are given in Figure 9. We have overlaid the SED for NGC 3190, which is characteristic of a region dominated by emission from grains in the diffuse ISM, and Mrk 33 which is characteristic of emission from grains in PDRs. We have  $24\mu\text{m}$  data for 57 sources. The emission between  $8\mu\text{m}$  and  $24\mu\text{m}$  in the ISFOs is a mix of these two templates.

For the 41 ISFOs with  $24\mu\text{m}$  detections we can estimate  $f_{Intense}$  directly, and for an additional 16 ISFOs the  $24\mu\text{m}$  limit is consistent with a  $\leq 10\%$   $f_{Intense}$ . Two thirds (37/57) of the ISFOs are dominated by emission from the diffuse ISM with a  $\lesssim 10\%$  contribution from PDRs based on their  $8 - 24\mu\text{m}$  emission. One in six ISFOs have a significant PDR component, with  $f_{Intense} \sim 30\%$  in Arp 72-S2 through Arp 72-S5, Arp82-S2, Arp 82-S4, NGC 5291-13, NGC 5291-26 (TDG-N), NGC5291-28, and  $f_{Intense} \sim 60\%$  in Arp 82-N1. This is comparable to SINGS, where one in seven galaxies have  $f_{Intense} \gtrsim 30\%$  (Draine et al. 2007).

ISFOs with  $f_{Intense} \geq 30\%$  tend to have a red  $[4.5] - [8.0]$  color. However the reddest ISFOs ( $[4.5] - [8.0] > 3.7$ ) are not correlated with  $f_{Intense}$ . The PAH emission in ISFOs is predominantly from a diffuse ISM.

## 5. Summary

We have investigated a sample of 67 ISFOs from 14 systems, consisting of 13 interacting galaxy pairs and Stephan’s Quintet. The ISFOs range from classical TDGs at the tips of tidal tails, groups of sources that together define “beads-on-a-string”, plus a luminous “hinge clump” at the base of a tidal feature. In the introduction we posed a number of questions concerning the mid-infrared properties of ISFOs. Here we summarize our response to those questions.

Spitzer IRS observations of 10 ISFOs in Arp 72, Arp 82, Arp 84, Arp 87, Arp 105, Arp 242, Arp 284, NGC 5291 and Stephan’s Quintet indicate that:

- 1) Two thirds of the ISFO sample have an  $R_{6/7}$  similar to the SINGS and starburst galaxies, which corresponds to the models with bright emission from large PAHs ( $N_C \sim 100$ ). In Arp 105-S2, Arp 82-N1 and Arp 284-SW1  $R_{6/7}$  is similar to what is observed in

BCDs and local giant HII regions, corresponding to the models with bright emission from small PAHs ( $N_C \leq 50$ ).

2) PAH models with the observed ISFO  $R_{11/7}$  indicate a mix of neutral and charged PAHs with  $\geq 50\%$  of the PAHs being neutral. The  $\langle R_{11/7} \rangle$  for the ISFOs is consistent with SINGS AGN and HII sources and starburst galaxies. Sources in the three local giant HII regions (NGC 3603, 30 Dor. and N 66) and BCDs tend to have a much larger fraction of neutral PAHs.

3) The  $[\text{Ne III}]/[\text{Ne II}]$  and  $[\text{S IV}]/[\text{S III}]$  line flux ratios are used as an excitation diagnostic and as a proxy for the slope of the ISRF in the UV. The ionized gas in the ISFOs indicates moderate levels of excitation with an ISRF that is harder than the majority of the SINGS and starburst galaxies but softer than BCDs and local giant HII regions. The neon line flux ratios are consistent with population synthesis models for recent star formation, i.e., a burst of star formation  $\lesssim 6$  million years ago. The wide range in the observed  $R_{11/7}$  for different galaxies for a given value of neon line flux ratio implies that  $R_{11/7}$  is driven by a change in the PAH ion fraction.  $\langle R_{8/7} \rangle = 0.20 \pm 0.05$  for 8 ISFOs, and is consistent with the  $\langle R_{8/7} \rangle$  observed in SINGS galaxies. The ionization fraction can drive the relative strengths of the PAH bands. As the PAH ion fraction increases and/or the PAH grain size increases the PAHs can absorb longer wavelength photons and the observed emission is less dependent on the hardness of the radiation field.

4) Emission from the low-J rotational lines from warm molecular hydrogen is detected in 88% (7/8) of the ISFOs corresponding to  $\sim 10^6 M_\odot$  of warm  $\text{H}_2$ .

Analysis of the IRAC and MIPS photometry for 67 ISFOs confirms that the ISFOs have a ‘notched-shaped’ SED, which is characteristic of star forming regions.

5) The ISFOs separate into two groups in  $[4.5] - [8.0]$  color. The blue group ( $[4.5] - [8.0] < 3$ ) has colors similar to SINGS galaxies. The red group is redder on average than normal spirals, dwarf irregulars and BCD galaxies. This is caused by bright emission at  $8 \mu\text{m}$ , most likely from PAHs. The observed color offsets between dwarfs and ISFOs when the  $[3.6] - [24.0]$  color is plotted as a function of either the  $[3.6] - [8.0]$ , or  $[8.0] - [24.0]$  color, are consistent with our spectroscopic results that show the majority of the ISFOs have a ISM with bright PAHs, illuminated by diffuse stellar light, in contrast to low metallicity dwarfs. ISFOs have colors similar to either star forming knots in the disks of interacting galaxies (red  $[4.5] - [8.0]$  color) or global properties of SINGS-HII galaxies (blue  $[3.6] - [8.0]$  color), but not the global properties of dwarf galaxies.

6) In two thirds (37/57) of the ISFOs the infrared power is dominated by emission from grains in the diffuse ISM illuminated by a ISRF with  $G_o \leq 10$ . One in six ISFOs have a

significant PDR component, with  $f_{Intense} \sim 30\%$  in Arp 72-S2 through Arp 72-S5, Arp82-S2, Arp 82-S4, NGC 5291-13, NGC 5291-26 (TDG-N), NGC5291-28, and  $f_{Intense} \sim 60\%$  in Arp 82-N1.

This paper compared the mid-infrared properties of ISFOs to other galaxy types and sources in local giant HII regions. The ISFOs are observed to have bright PAH emission with a significant fraction of PAH ions, that is located in a diffuse ISM. This is similar to what is observed in SINGS-HII galaxies. In contrast the relative PAH band strength in BCDs indicates a population of mainly neutral PAHs, consistent with the emission from sources in local giant HII regions, which are exposed to more intense stellar radiation fields.

This work is based [in part] on observations made with the Spitzer Space Telescope, which is operated by the Jet Propulsion Laboratory, California Institute of Technology under NASA contract 1407. Support for this work was provided by NASA through Contract Number 1257184 issued by JPL/Caltech. This research has made use of the excellent NASA/IPAC Extragalactic Database (NED) which is operated by the Jet Propulsion Laboratory, California Institute of Technology, under contract with the National Aeronautics and Space Administration; Partial funding for this work was provided by Spitzer/NASA grants RSA No.s 1346930 (Higdon & Higdon), 1353814 (Smith & Hancock). We thank Bruce Draine and the referee for constructive comments, which have improved this paper.

## REFERENCES

- Allamandola, L. J., Tielens, A. G. G. M. & Barker, J. R. 1985, ApJ, 290, L25
- Arp, H., 1966, ApJS, 14, 1
- Bakes, E. L. O., Tielens, A. G. G. M., Bauschlicher, C. et al. 2001, ApJ, 560, 261
- Bauschlicher, C. W., Peeters, E. & Allamandola, L. 2008, ApJ, 678, 316
- Beiraro, P., Appleton, P. N., Brandl, B. R. et al. 2009, ApJ, 693, 1650
- Boquien, M. et al. 2009, AJ, 137, 4561
- Boquien, M. et al. 2010, ApJ, 140, 2124
- Bournaud, F & Duc, P.-A. 2006, A&A, 456, 481
- Braine, J. et al. 2001, A&A, 378, 51
- Cluver, M. E., Appleton, P. N., Boulanger, F. et al. 2010, ApJ, 710, 248
- Cohen, M., Megeath, T.G., Hammersley, P.L. et al. 2003, AJ, 125, 2645

- Cutri, R. et al. 2003, The IRSA 2MASS All-Sky Point Source Catalog, NASA/IPAC Infrared Science Archive
- Dale, D. A., Bendo, G. J., Engelbracht, C. W. et al. 2005 ApJ, 633, 857
- Decin, L., Morris, P. W., Appleton, P. N. et al. 2004, ApJS, 154, 408
- de Mello, D. F., Urrutia-Viscarra, F., Mendes de Oliveira, C et al. 2012, MNRAS, 426, 2441
- Draine, B. T., Dale, D. A., Bendo, G., et al. 2007, ApJ, 663, 866
- Draine, B. T. & Li, A. 2001, ApJ, 551, 807
- Draine, B. T. & Li, A. 2007, ApJ, 657, 810
- Duc, P.-A. & Mirabel, I. 1994, A&A, 289, 83
- Duc, P.-A. & Mirabel, I. 1998, A&A, 333, 813
- Duc, P.-A. & Paudel, S., McDermid, R., et al. 2014, MNRAS, Accepted
- Duc, P.-A. et al. 2014, MNRAS, 440, 1458
- Elmegreen, B. G. & Efremov, Y. N. 1996, ApJ, 466, 802
- Elmegreen, B. G., Kaufman, M., & Thomasson, M. 1993, ApJ, 412, 90
- Engelbracht, C. W., Gordon, K. D., Rieke, G. H., et al. 2005, ApJ, 628, 29
- Engelbracht, C. W. et al. 2007, PASP, 119, 994
- Fazio, G., Ashby, M., Barmby, P., et al. 2004a, ApJ, 154, 39
- Fazio, G. G., Hora, J. L., Allen, L. E. et al., 2004b, ApJS, 154, 10
- Galliano, F., Madden, S. C., Jones, A. P. et al. 2003, A&A, 407, 159
- Galliano, F. et al. 2008, ApJ, 679, 310
- Gordon, K. et al. 2008, ApJ, 682, 336
- Habing, H. J. 1968, BAN, 19, 421
- Hancock, M., Smith, B. J., Struck, C. et al., 2007, AJ, 133, 676
- Hibbard, J., Guhathakurta, P., van Gorkom, J., & Schweizer, F. 1994, AJ, 107, 67
- Hibbard, J. E. & Mihos, J. C. 1995, AJ, 110, 140
- Hibbard, J. E. & van Gorkom, J. H. 1996, AJ, 111, 655
- Higdon, S. J. U., Armus, L., Higdon, J. L. et al. 2006a, ApJ, 648, 323
- Higdon, S. J. U., Devost, D., Higdon, J. L. et al. 2004, PASP, 116, 975

- Higdon, S. J. U., & Higdon, J. L. 2008, in IAU Symp. 244 Dark Galaxies and Lost Baryons, ed. J. I. Davies & M. J. Disney (Cambridge, Cambridge Univ. Press), 356
- Higdon, S. J. U., Higdon, J. L., & Marshall, J. HHM06 2006b, ApJ, 640, 768
- Higdon, S. J. U., Higdon, J. L., Smith, B. J., Hancock, M., Struck, C. 2010, in ASP Conf. Ser. 423, Galaxy Wars: Stellar Populations and Star Formation in Interacting Galaxies, ed. Smith, B. J., Bastian, N. Higdon, S. J. U. & Higdon, J. L. (San Francisco, CA:ASP), 271
- Houck, J. R., Charmandaris, V, Brandl, B et al., 2004a ApJS, 154, 211
- Houck, J. R., Roellig, T., Van Cleve, J. et al. 2004b ApJS, 154, 18
- Hunsberger, S. D., Charlton, J., & Zaritsky, D. 1996, ApJ, 462, 50
- Hunt, L. K., Thuan, T., Izotov, Y. & Sauvage, M. 2010, ApJ, 712, 164
- Kaviraj, S., Darg, D., Lintott, C., Schawinski, K. & Silk, J. 2012, MNRAS, 419, 70
- Kennicutt, R. C., Armus, L., Bendo, G. et al. 2003, PASP, 115, 928
- Lapham, R., Smith, B. & Struck, C. 2013, AJ, 145, 130
- Lebouteiller, V. et al. 2011, ApJ, 728, 45
- Li, A & Draine, B. T. 2001, ApJ, 554, 778
- Longmore, A. J., Hawarden, T. G., Cannon, R. D., et al. 1979 MNRAS, 188, 285 (L79)
- Madden, S. C. 2000, NewAR, 44, 249
- Madden, S. C., Galliano, F., Jones, A. P. & Sauvage, M. 2006, A&A, 446, 877
- Makovoz, D., & Marleau, F. R. 2005, PASP, 117, 1113
- Mirabel, I. F., Lutz, D., & Maza, J. 1991, A&A, 243, 367
- Morris, S. L. & van den Bergh, S. 1994, ApJ, 427, 696
- Pena, M., Ruiz, M. T. & Maza, J. 1991, A&A, 251, 417
- Petitpas, G. R. & Taylor, C. L. 2005, ApJ, 633, 138
- Plante, S & Sauvage, M. 2002, AJ, 124, 1995
- Reach, W. et al. 2005, PASP, 117, 978
- Rieke, G. H., Young, E. T., Engelbracht, C. W. et al. 2004, ApJS, 154, 25
- Rosenberg, J. L., Ashby, M. L. N., Salzer, J. J. & Huang, J. -S. 2006, ApJ, 636, 742
- Rosenberg, J. L., et al. 2008, ApJ, 674, 814

- Sanders, D. B. & Mirabel, I. F. 1996, ARAA, 34, 749
- Schutte, W. A., Tielens, A. G. G. M., & Allamandola 1993 ApJ, 415, 397
- Schweizer, F. 1978, in Structure and Properties of Nearby Galaxies, ed. E. M. Berkhuijsen & R. Wielebinski (Dordrecht: Reidel), 279.
- Schombert, J. M., Wallin, J. F. & Struck-Marcell, C. 1990, ApJ, 99, 497
- Smith, B. J., Giroux, M. L., & Struck, C., et al. 2010, AJ, 139, 1212
- Smith, B. J. & Hancock, M. 2009, AJ, 138, 130
- Smith, B. J. & Struck, C. 2012, MNRAS, 422, 2444
- Smith, B. J., Struck, C., Hancock, M., et al. 2007a, AJ, 133, 791
- Smith, B. J., Struck, C., Hancock, M., et al. 2008, AJ, 135, 2406
- Smith, J. D. T., Draine, B. T., Dale, D. A. et al. 2007b, ApJ, 656, 770
- Struck, C. & Smith, B. J. 2003, ApJ, 589, 157
- Struck, C. & Smith, B. 2012, MNRAS, 422, 2444
- Thornley, M. D., Forster Schreiber, M., Lutz, et al. 2000, ApJ 539 641
- Thuan, T. X., Sauvage, M. & Madden, S. 1999, ApJ, 516, 783
- Toomre, A. & Toomre, J. 1972, ApJ, 178, 623
- Van der Hulst, J. M., 1979, A&A, 71, 131
- Verley, S., Hunt, L. K., Corbelli, E., & Giovanardi, C. 2007 A&A, 476, 1161
- Verma, A. Lutz, D., Sturm, E., et al. 2003, A&A, 403, 829
- Weilbacher, P. M., Duc, P.-A., & Fritze-v. Alvensleben, U. 2003, A&A, 397, 545
- Weingartner, J. C., & Draine, B. T. 2001, ApJ, 563, 842
- Wu, Y., Charmandaris, V., Hunt, L. K. et al. 2007, ApJ, 662, 952
- Zwicky, F. 1956, Ergebnisse der Exakten Naturwissenschaften, 29, 344

Table 1. Spitzer 8  $\mu$ m ISFOs

Object	RA (J2000) h:m:s	Dec (J2000) °:′:″	D Mpc
Arp 65-N1	00:21:47.74	+22:24:55.9	75.4
Arp 65-N2	00:21:49.43	+22:24:41.2	75.4
Arp 65-N3	00:21:50.18	+22:24:34.5	75.4
Arp 65-N4	00:21:50.74	+22:24:26.3	75.4
Arp 65-S1	00:21:51.53	+22:23:38.4	75.4
Arp 65-S2	00:21:53.48	+22:23:27.9	75.4
Arp 65-S3	00:21:53.14	+22:23:27.9	75.4
Arp 72-S1	15:46:58.24	+17:52:32.7	46.5
Arp 72-S2	15:46:57.02	+17:52:22.1	46.5
Arp 72-S3	15:46:57.47	+17:52:27.2	46.5
Arp 72-S4	15:46:57.02	+17:52:22.9	46.5
Arp 72-S5	15:46:56.77	+17:52:19.4	46.5
Arp 82-N1	08:11:13.93	+25:13:09.6	57.7
Arp 82-S1	08:11:12.56	+25:11:40.9	57.7
Arp 82-S2	08:11:12.97	+25:11:25.7	57.7
Arp 82-S3	08:11:13.06	+25:11:21.2	57.7
Arp 82-S4	08:11:14.02	+25:11:13.8	57.7
Arp 84-N1	13:58:33.52	+37:27:42.3	48.9
Arp 87-N1	11:40:45.11	+22:25:58.8	100.2
Arp 102-N1	17:19:17.20	+49:04:45.2	101.8
Arp 102-N2	17:19:17.14	+49:04:38.7	101.8
Arp 104-S1	13:32:01.69	+62:41:32.9	45.7
Arp 105-N1	11:11:12.68	+28:45:55.0	123.6
Arp 105-N2	11:11:12.59	+28:45:37.6	123.6
Arp 105-S1	11:11:13.37	+28:41:24.6	123.6
Arp 105-S2	11:11:13.46	+28:41:16.3	123.6
Arp 107-E1	10:52:14.78	+30:04:06.5	140.1
Arp 107-SW1	10:52:12.82	+30:03:49.6	140.1
Arp 107-N1	10:52:12.63	+30:04:21.5	140.1
Arp 242-N1	12:46:10.45	+30:45:31.0	93.1
Arp 242-N2	12:46:10.45	+30:45:22.6	93.1
Arp 242-N3	12:46:10.46	+30:45:12.1	93.1
Arp 242-N4	12:46:10.55	+30:45:04.0	93.1
Arp 242-N5	12:46:10.46	+30:44:53.2	93.1
Arp 242-N6	12:46:10.42	+30:44:34.0	93.1
Arp 242-N7	12:46:10.37	+40:44:26.2	93.1



Table 1—Continued

Object	RA (J2000) h:m:s	Dec (J2000) °:′:″	D Mpc
Arp 242-N8	12:46:10.33	+30:44:20.8	93.1
Arp 284-E1	23:36:18.53	+02:09:26.5	39.5
Arp 284-SW1	23:36:13.37	+02:09:03.7	39.5
Arp 284-SW2	23:36:12.96	+02:09:01.7	39.5
Arp 285-N1	09:24:18.49	+49:15:18.6	27.9
SQ-A	22:35:58.91	+33:58:49.5	90.8
SQ-B	22:36:10.38	+33:57:20.0	90.8
NGC 5291-13	12:46:10.45	-30:45:31.0	62.0
NGC 5291-15	12:46:10.45	-30:45:31.0	62.0
NGC 5291-16	12:46:10.45	-30:45:31.0	62.0
NGC 5291-17	12:46:10.45	-30:45:31.0	62.0
NGC 5291-18	12:46:10.45	-30:45:31.0	62.0
NGC 5291-19	12:46:10.45	-30:45:31.0	62.0
NGC 5291-22	12:46:10.45	-30:45:31.0	62.0
NGC 5291-25	12:46:10.45	-30:45:31.0	62.0
NGC 5291-26	12:46:10.45	-30:45:31.0	62.0
NGC 5291-28	12:46:10.45	-30:45:31.0	62.0
NGC 5291-30	12:46:10.45	-30:45:31.0	62.0
NGC 5291-31	12:46:10.45	-30:45:31.0	62.0
NGC 5291-32	12:46:10.45	-30:45:31.0	62.0
NGC 5291-33	12:46:10.45	-30:45:31.0	62.0
NGC 5291-36	12:46:10.45	-30:45:31.0	62.0
NGC 5291-39	12:46:10.45	-30:45:31.0	62.0
NGC 5291-41	12:46:10.45	-30:45:31.0	62.0
NGC 5291-42	12:46:10.45	-30:45:31.0	62.0
NGC 5291-43	12:46:10.45	-30:45:31.0	62.0
NGC 5291-45	12:46:10.45	-30:45:31.0	62.0
NGC 5291-47	12:46:10.45	-30:45:31.0	62.0
NGC 5291-49	12:46:10.45	-30:45:31.0	62.0
NGC 5291-50	12:46:10.45	-30:45:31.0	62.0
NGC 5291-51	12:46:10.45	-30:45:31.0	62.0

Table 2. Spitzer Photometry

Object	$F_{3.6\mu m}$ $\mu Jy$	$F_{4.5\mu m}$ $\mu Jy$	$F_{5.8\mu m}$ $\mu Jy$	$F_{8\mu m}$ $\mu Jy$	$F_{24\mu m}$ $\mu Jy$	Aper <sup>a</sup>
Arp 65-N1	$29.3 \pm 4.5$	$17.6 \pm 3.6$	$46.3 \pm 6.8$	$181.4 \pm 11.8$	$\leq 113.7$	3,2
Arp 65-N2	$36.2 \pm 5.0$	$24.4 \pm 4.2$	$67.9 \pm 7.3$	$157.9 \pm 11.2$	$\leq 132.5$	2,2
Arp 65-N3	$29.4 \pm 4.9$	$17.6 \pm 3.5$	$68.0 \pm 7.3$	$154.8 \pm 11.1$	$\leq 169.0$	2,2
Arp 65-N4	$45.1 \pm 5.6$	$26.7 \pm 4.3$	$62.4 \pm 7.1$	$176.0 \pm 11.8$	$\leq 184.1$	2,2
Arp 65-S1	$157.2 \pm 5.2$	$108.7 \pm 4.5$	$244.4 \pm 6.7$	$615.5 \pm 11.9$	$848.5 \pm 64.6$	3,2
Arp 65-S2 <sup>b</sup>	$34.5 \pm 2.9$	$15.4 \pm 2.8$	$73.5 \pm 6.6$	$283.9 \pm 6.4$	$346.2 \pm 41.2$	2,2
Arp 65-S3 <sup>b</sup>	$39.4 \pm 3.0$	$28.8 \pm 2.8$	$95.1 \pm 8.1$	$276.8 \pm 6.4$	$346.2 \pm 41.2$	2,2
Arp 72-S1	$690.2 \pm 7.3$	$520.1 \pm 6.6$	$1927.7 \pm 13.3$	$5425.9 \pm 14.0$	$13148.0 \pm 248.0$	3,2
Arp 72-S2	$234.3 \pm 13.3$	$157.5 \pm 11.3$	$558.8 \pm 20.1$	$1649.6 \pm 35.6$	$5149.6 \pm 156.3$	2,2
Arp 72-S3	$189.5 \pm 11.4$	$135.5 \pm 9.7$	$435.3 \pm 17.6$	$1192.5 \pm 30.4$	$4101.4 \pm 166.2$	2,2
Arp 72-S4	$149.7 \pm 10.1$	$101.0 \pm 8.9$	$326.9 \pm 15.5$	$861.3 \pm 26.7$	$2938.4 \pm 142.7$	2,2
Arp 72-S5	$125.3 \pm 9.3$	$92.2 \pm 7.9$	$279.3 \pm 14.4$	$712.1 \pm 23.7$	$2502.8 \pm 130.1$	2,2
Arp 82-N1	$259.3 \pm 5.0$	$225.8 \pm 4.3$	$973.4 \pm 9.8$	$2906.1 \pm 16.1$	$20926.1 \pm 260.0$	2,3
Arp 82-S1	$146.9 \pm 4.3$	$103.3 \pm 4.8$	$428.5 \pm 11.0$	$1271.7 \pm 14.7$	$3388.6 \pm 131.0$	2,1
Arp 82-S2	$144.1 \pm 9.4$	$86.0 \pm 7.6$	$298.3 \pm 18.9$	$912.1 \pm 23.8$	$3079.1 \pm 120.5$	2,2
Arp 82-S3	$93.8 \pm 7.6$	$49.0 \pm 6.0$	$175.3 \pm 12.3$	$540.9 \pm 20.4$	$1557.1 \pm 91.9$	2,2
Arp 82-S4	$60.3 \pm 6.1$	$34.5 \pm 5.2$	$143.8 \pm 11.5$	$453.2 \pm 18.8$	$1575.6 \pm 92.3$	2,2
Arp 84-N1 <sup>c</sup>	$371.3 \pm 4.4$	$251.5 \pm 4.9$	$850.9 \pm 19.2$	$2626.3 \pm 15.3$	...	3,-
Arp 87-N1 <sup>c</sup>	$139.9 \pm 6.2$	$96.7 \pm 4.7$	$226.2 \pm 13.1$	$854.4 \pm 18.1$	...	3,-
Arp 102-N1	$63.7 \pm 13.5$	$57.8 \pm 12.9$	$\leq 27.4$	$176.9 \pm 24.0$	$218.8 \pm 27.7$	1,1
Arp 102-N2	$347.9 \pm 30.9$	$202.2 \pm 23.7$	$111.4 \pm 18.7$	$47.7 \pm 13.5$	$\leq 83.5$	4,1
Arp 104-S1	$239.3 \pm 6.6$	$184.6 \pm 4.7$	$109.0 \pm 12.2$	$391.9 \pm 12.8$	$622.7 \pm 56.0$	3,1
Arp 105-N1	$201.8 \pm 10.4$	$144.2 \pm 8.7$	$331.4 \pm 20.3$	$617.7 \pm 23.7$	...	6,-
Arp 105-N2	$19.0 \pm 4.7$	$23.4 \pm 4.1$	$68.9 \pm 10.3$	$235.3 \pm 12.0$	...	3,-
Arp 105-S1	$47.8 \pm 5.8$	$30.9 \pm 4.2$	$92.1 \pm 10.4$	$277.1 \pm 13.1$	...	1,-
Arp 105-S2	$336.4 \pm 10.9$	$271.0 \pm 10.4$	$677.7 \pm 20.6$	$1970.7 \pm 24.9$	...	4,-
Arp 107-E1	$349.9 \pm 7.9$	$203.8 \pm 7.4$	$648.2 \pm 18.2$	$2586.2 \pm 18.4$	$2184.9 \pm 36.5$	5,1
Arp 107-SW1	$124.4 \pm 5.2$	$83.2 \pm 4.1$	$340.3 \pm 11.6$	$1219.3 \pm 16.2$	$889.2 \pm 35.0$	3,1
Arp 107-N1	$85.4 \pm 5.8$	$49.7 \pm 5.5$	$63.3 \pm 10.5$	$177.6 \pm 13.1$	$105.5 \pm 37.0$	3,1
Arp 242-N1	$90.0 \pm 8.6$	$52.9 \pm 5.9$	$101.6 \pm 9.8$	$233.3 \pm 14.2$	$263.5 \pm 46.1$	2,1
Arp 242-N2	$267.1 \pm 14.5$	$154.2 \pm 10.7$	$165.7 \pm 19.5$	$403.6 \pm 13.7$	$\leq 120.0$	3,1
Arp 242-N3	$428.6 \pm 4.2$	$267.3 \pm 4.2$	$407.8 \pm 13.2$	$946.7 \pm 14.7$	$536.3 \pm 44.1$	3,1
Arp 242-N4	$163.5 \pm 2.7$	$85.4 \pm 2.6$	$107.3 \pm 9.2$	$286.5 \pm 11.0$	$\leq 120.0$	2,1
Arp 242-N5	$411.0 \pm 4.3$	$254.2 \pm 4.5$	$243.5 \pm 14.3$	$558.2 \pm 12.8$	$369.2 \pm 54.6$	3,1

Table 2—Continued

Object	$F_{3.6\mu m}$ $\mu Jy$	$F_{4.5\mu m}$ $\mu Jy$	$F_{5.8\mu m}$ $\mu Jy$	$F_{8\mu m}$ $\mu Jy$	$F_{24\mu m}$ $\mu Jy$	Aper <sup>a</sup>
Arp 242-N6	$503.5 \pm 4.7$	$315.7 \pm 4.2$	$548.3 \pm 14.9$	$1277.1 \pm 19.0$	$1555.1 \pm 82.0$	3,1
Arp 242-N7	$239.7 \pm 3.2$	$149.8 \pm 2.9$	$252.8 \pm 10.1$	$567.5 \pm 11.6$	$\leq 120.0$	2,1
Arp 242-N8	$236.8 \pm 4.6$	$144.7 \pm 3.8$	$232.3 \pm 11.4$	$587.3 \pm 10.1$	$\leq 120.0$	2,1
Arp 284-E1 <sup>c</sup>	$61.1 \pm 5.8$	$47.6 \pm 7.1$	$219.9 \pm 15.2$	$721.8 \pm 16.5$	...	3,-
Arp 284-SW1 <sup>c</sup>	$524.6 \pm 8.1$	$432.4 \pm 6.6$	$1217.7 \pm 16.6$	$3177.9 \pm 18.8$	...	2,-
Arp 284-SW2 <sup>c</sup>	$282.5 \pm 6.6$	$205.7 \pm 6.9$	$917.6 \pm 20.0$	$2513.5 \pm 16.6$	...	2,-
Arp 285-N1	$23.0 \pm 3.5$	$17.5 \pm 3.6$	$64.4 \pm 12.1$	$353.9 \pm 18.7$	...	2,-
SQ-A	$458.5 \pm 15.8$	$328.5 \pm 12.1$	$1271.8 \pm 29.9$	$3695.2 \pm 43.9$	$9308.7 \pm 23.2$	4,3
SQ-B	$260.2 \pm 9.6$	$186.8 \pm 8.0$	$831.6 \pm 21.1$	$2553.4 \pm 39.9$	$5717.3 \pm 25.3$	4,3
NGC 5291-13	$140.0 \pm 3.5$	$107.0 \pm 3.4$	$170.0 \pm 15.2$	$419.0 \pm 10.2$	$1978.1 \pm 55.9$	3,3
NGC 5291-15	$39.9 \pm 3.5$	$29.1 \pm 3.4$	$86.6 \pm 15.2$	$252.0 \pm 10.2$	$429.0 \pm 36.5$	3,3
NGC 5291-16	$145.0 \pm 3.5$	$122.0 \pm 3.4$	$92.3 \pm 15.1$	$231.0 \pm 10.2$	$396.7 \pm 47.8$	3,3
NGC 5291-17	$89.9 \pm 3.5$	$57.1 \pm 3.4$	$259.0 \pm 15.2$	$663.0 \pm 10.2$	$656.7 \pm 49.4$	3,3
NGC 5291-18	$45.0 \pm 3.5$	$24.8 \pm 3.4$	$130.0 \pm 15.2$	$352.0 \pm 10.3$	$505.1 \pm 36.7$	3,3
NGC 5291-19	$30.7 \pm 3.5$	$9.6 \pm 3.4$	$\leq 36.3$	$188.0 \pm 10.2$	$\leq 146.1$	3,3
NGC 5291-22	$49.5 \pm 2.6$	$32.1 \pm 2.9$	$40.7 \pm 10.8$	$106.0 \pm 9.2$	$173.7 \pm 33.8$	3,3
NGC 5291-25	$69.3 \pm 2.6$	$38.0 \pm 2.9$	$402.0 \pm 10.8$	$486.0 \pm 9.2$	$778.7 \pm 48.4$	3,3
NGC 5291-26	$513.0 \pm 6.5$	$389.3 \pm 6.2$	$1844.5 \pm 28.2$	$4804.0 \pm 18.8$	$14809.2 \pm 76.1$	3,3
NGC 5291-28	$19.8 \pm 2.6$	$8.1 \pm 2.9$	$18.9 \pm 10.9$	$71.1 \pm 9.3$	$306.5 \pm 32.1$	3,3
NGC 5291-30	$373.0 \pm 3.5$	$256.0 \pm 3.4$	$286.0 \pm 15.2$	$1350.0 \pm 10.3$	$943.2 \pm 35.3$	3,3
NGC 5291-31	$8.9 \pm 2.6$	$10.4 \pm 2.9$	$52.3 \pm 10.9$	$158.9 \pm 9.2$	$\leq 135.2$	3,3
NGC 5291-32	$118.0 \pm 3.5$	$72.5 \pm 3.4$	$300.0 \pm 15.2$	$853.0 \pm 10.2$	$778.0 \pm 37.9$	3,3
NGC 5291-33	$295.0 \pm 6.5$	$160.9 \pm 6.1$	$617.8 \pm 28.2$	$1930.0 \pm 18.8$	$2233.6 \pm 37.0$	3,3
NGC 5291-36	$27.4 \pm 2.6$	$17.8 \pm 2.9$	$28.4 \pm 10.9$	$174.0 \pm 9.2$	$\leq 130.0$	3,3
NGC 5291-39	$17.1 \pm 2.6$	$15.0 \pm 2.9$	$27.3 \pm 10.8$	$113.0 \pm 9.3$	$\leq 107.0$	3,3
NGC 5291-41	$25.0 \pm 2.6$	$10.8 \pm 2.9$	$40.0 \pm 10.9$	$137.0 \pm 9.2$	$196.9 \pm 30.9$	3,3
NGC 5291-42	$51.0 \pm 3.5$	$32.7 \pm 3.4$	$105.0 \pm 15.2$	$258.0 \pm 10.2$	$212.7 \pm 34.5$	3,3
NGC 5291-43	$62.8 \pm 2.6$	$40.5 \pm 2.9$	$62.1 \pm 10.9$	$180.0 \pm 9.2$	$217.7 \pm 34.5$	3,3
NGC 5291-45	$76.0 \pm 2.6$	$62.0 \pm 2.9$	$25.1 \pm 10.8$	$198.0 \pm 9.2$	$\leq 110.7$	3,3
NGC 5291-47	$38.6 \pm 2.6$	$17.3 \pm 2.9$	$97.6 \pm 10.8$	$284.0 \pm 9.2$	$379.4 \pm 35.5$	3,3
NGC 5291-49	$27.5 \pm 2.6$	$15.1 \pm 2.9$	$50.1 \pm 10.8$	$158.0 \pm 9.2$	$\leq 121.1$	3,3
NGC 5291-50	$27.7 \pm 2.6$	$21.0 \pm 2.9$	$57.2 \pm 10.8$	$162.0 \pm 9.3$	$166.0 \pm 37.4$	3,3
NGC 5291-51	$134.0 \pm 2.6$	$88.9 \pm 2.9$	$142.0 \pm 10.8$	$313.0 \pm 9.2$	$256.0 \pm 37.0$	3,3

<sup>a</sup>Aperture and sky annulus radii code. The first integer refers to IRAC observations and the second integer refers to MIPS. A dash indicates that no data was available. The IRAC code is: 1-(3'', 3–7''), 2-(3'', 10–20''), 3-(5'', 10–20''), 4-(6'', 10–20''), 5-(8'', 10–20''), 6-(10'', 10–20''), 7-(13'', 20–32''). The aperture code for MIPS is: 1-(6'', 20–32''), 2-(6.6'', 20–32), 3-(13'', 20–32'').

<sup>b</sup>Two sources are visible in IRAC but only one in MIPS. We divide the 24 $\mu$ m flux equally between them

<sup>c</sup>ISFOs are buried by bright emission (diffraction patterns) from main galaxy at 24 $\mu$ m.

Table 3. Aperture Scale Factors<sup>a</sup>

Module	Arp 72 S1	Arp 82 N1	Arp 84 N1 <sup>b</sup>	Arp 87 N1 <sup>b</sup>	Arp 105 S2	Arp 242 N3	Arp 284 SW1 <sup>b</sup>	NGC 5291 N <sup>c</sup>	NGC 5291 S <sup>c</sup>	SQA
SL	1.69	0.87	1.41	1.0	1.19	1.43	0.90	1.04	1.72	4.25
LL	0.76	0.95	0.64	0.24	...	...	...	...	...	...
SH	4.0	0.94	2.81	0.34	...	...	0.76	...	...	7.41
LH	0.63	0.78	0.49	0.23	...	...	0.40	...	...	...

<sup>a</sup>Apertures listed in Table 2

<sup>b</sup>No MIPS 24 $\mu$ m photometry

<sup>c</sup>No sky data available for HIRES see HHM06

Table 4. Line Flux

Line <sup>a</sup>	Arp 72 S1 <sup>b</sup>	Arp 82 N1 <sup>c</sup>	Arp 84 N1	Arp 87 N1	Arp 284 SW1	NGC 5291N <sup>d</sup>	NGC 5291S <sup>d</sup>	SQA
[SIV]	11.61 <sup>+</sup> <sub>-0.94</sub>	8.80 <sup>+</sup> <sub>-0.46</sub>	$\leq 4.50$	...	5.51 <sup>+</sup> <sub>-0.49</sub>	7.40 <sup>+</sup> <sub>-0.15</sub>	1.05 <sup>+</sup> <sub>-0.22</sub>	7.66 <sup>+</sup> <sub>-2.16</sub>
10.51 $\mu$ m	-0.16	-0.15	...	...	-0.05	-0.02	-0.00	-0.05
[NeII]	13.34 <sup>+</sup> <sub>-5.71</sub>	15.35 <sup>+</sup> <sub>-0.73</sub>	5.29 <sup>+</sup> <sub>-0.34</sub>	0.99 <sup>+</sup> <sub>-0.05</sub>	15.97 <sup>+</sup> <sub>-0.54</sub>	10.65 <sup>+</sup> <sub>-0.06</sub>	4.05 <sup>+</sup> <sub>-0.31</sub>	26.24 <sup>+</sup> <sub>-2.20</sub>
12.81 $\mu$ m	-0.09	-0.17	-0.13	-0.02	-0.02	-0.02	-0.01	-0.22
[NeIII]	21.74 <sup>+</sup> <sub>-4.99</sub>	30.30 <sup>+</sup> <sub>-0.49</sub>	1.34 <sup>+</sup> <sub>-0.25</sub>	0.51 <sup>+</sup> <sub>-0.17</sub>	31.14 <sup>+</sup> <sub>-0.44</sub>	25.31 <sup>+</sup> <sub>-1.03</sub>	5.47 <sup>+</sup> <sub>-0.11</sub>	35.37 <sup>+</sup> <sub>-2.60</sub>
15.55 $\mu$ m	-0.31	-0.46	-0.07	-0.10	-0.56	-0.06	-0.02	-0.60
[SIII]	15.45 <sup>+</sup> <sub>-1.66</sub>	17.90 <sup>+</sup> <sub>-0.52</sub>	2.20 <sup>+</sup> <sub>-0.44</sub>	0.71 <sup>+</sup> <sub>-0.18</sub>	19.44 <sup>+</sup> <sub>-0.76</sub>	15.45 <sup>+</sup> <sub>-0.58</sub>	4.66 <sup>+</sup> <sub>-0.17</sub>	23.26 <sup>+</sup> <sub>-3.18</sub>
18.71 $\mu$ m	-0.21	-0.23	-0.20	-0.54	-0.25	-0.04	-0.01	-0.35
[SIII]	1.55 <sup>+</sup> <sub>-0.17</sub>	3.64 <sup>+</sup> <sub>-0.32</sub>	...	...	4.78 <sup>+</sup> <sub>-0.08</sub>	...	...	...
33.48 $\mu$ m	-0.21	-0.23	...	...	-0.24	...	...	...
[SiII]	1.66 <sup>+</sup> <sub>-0.40</sub>	1.96 <sup>+</sup> <sub>-0.61</sub>	...	...	...	...	...	...
34.81 $\mu$ m	-0.13	...	...	...	...	...	...	...
H <sub>2</sub> S2	$\leq 8.4$	$\leq 1.95$	$\leq 1.29$	0.40 <sup>+</sup> <sub>-0.13</sub>	$\leq 1.35$	1.90 <sup>+</sup> <sub>-0.80</sub>	0.90 <sup>+</sup> <sub>-0.40</sub>	$\leq 3.09$
12.28 $\mu$ m	...	...	...	-0.04	...	-0.00	-0.00	-0.04
H <sub>2</sub> S1	3.1 <sup>+</sup> <sub>-0.9</sub>	2.57 <sup>+</sup> <sub>-0.84</sub>	$\leq 2.04$	0.80 <sup>+</sup> <sub>-0.21</sub>	3.01 <sup>+</sup> <sub>-0.37</sub>	1.10 <sup>+</sup> <sub>-0.40</sub>	1.30 <sup>+</sup> <sub>-0.30</sub>	14.07 <sup>+</sup> <sub>-3.47</sub>
17.03 $\mu$ m	...	-0.02	...	-0.14	-0.04	-0.00	-0.00	-0.22
H <sub>2</sub> S0	$\leq 0.31$	7.48 <sup>+</sup> <sub>-1.50</sub>	...	...	...	...	...	...
28.22 $\mu$ m	...	-0.05	...	...	...	...	...	...

<sup>a</sup>[ W cm<sup>-2</sup>] scaled by 10<sup>22</sup>. Negative equivalent widths [ $\mu$ m] denote line emission.

<sup>b</sup>The molecular mass is calculated using the line fluxes measured in the IRS-LORES spectrum: H<sub>2</sub> S0 = (4.01<sup>+</sup><sub>-0.4</sub>) 10<sup>22</sup>W cm<sup>-2</sup>, H<sub>2</sub> S1 = (3.1<sup>+</sup><sub>-0.9</sub>) 10<sup>22</sup>W cm<sup>-2</sup>, H<sub>2</sub> S2 = (8.0<sup>+</sup><sub>-1.7</sub>) 10<sup>22</sup>W cm<sup>-2</sup>.

<sup>c</sup>The lines are blueshifted wrt to the rest wavelength for Arp 82 by  $\sim 200$  km s<sup>-1</sup>. The molecular mass is calculated using the HIRES fluxes for the H<sub>2</sub> S0 and S1 lines and the IRS-LORES fluxes for the H<sub>2</sub> S2 = (2.6<sup>+</sup><sub>-0.3</sub>) 10<sup>22</sup>W cm<sup>-2</sup>, H<sub>2</sub> S3 = (4.1<sup>+</sup><sub>-1.0</sub>) 10<sup>22</sup>W cm<sup>-2</sup>.

<sup>d</sup>data from HHM06

Table 5. PAH Flux

Flux <sup>a</sup> EW <sup>c</sup>	Arp 72 <sup>b</sup> S1	Arp 82 <sup>b</sup> N1	Arp 84 N1	Arp 87 N1	Arp 105 S2	Arp 242 N3	Arp 284 SW1	SQ A	NGC 5291 N	NGC 5291 S
P <sub>6,2</sub> Flux	13.89 ± 0.09	11.98 ± 2.70	7.37 ± 0.35	2.95 ± 0.10	6.60 ± 0.09	2.58 ± 0.46	9.66 ± 0.15	...	12.0 ± 0.6	5.09 ± 0.30
P <sub>6,2</sub> EW	-2.1	-6.0	-4.2	-3.5	-5.9	-4.1	-3.1	...	-8.3	-5.8
P <sub>7,7C</sub> Flux	48.28 ± 0.92	18.32 ± 4.35	22.22 ± 1.53	9.89 ± 0.74	14.46 ± 0.35	7.69 ± 0.20	23.82 ± 0.97	36.51 ± 0.25	42.40 ± 0.51	17.77 ± 0.64
P <sub>7,7C</sub> EW	-6.8	-5.7	-8.3	-12.9	-8.0	-12.2	-4.3	-90.6	-12.1	-10.0
P <sub>8,3</sub> Flux	4.40 ± 0.53	3.32 ± 1.63	3.20 ± 0.34	1.24 ± 0.25	1.54 ± 0.09	0.66 ± 0.13	2.38 ± 0.20	5.48 ± 0.11	2.67 ± 0.21	2.68 ± 0.17
P <sub>8,3</sub> EW	-0.6	-0.9	-1.1	-1.8	-0.7	-1.1	-0.4	-7.3	-0.6	-1.3
P <sub>8,6</sub> Flux	8.51 ± 0.50	3.59 ± 0.44	3.40 ± 0.11	1.02 ± 0.08	2.88 ± 0.06	2.17 ± 0.03	4.59 ± 0.26	10.54 ± 0.21	11.45 ± 0.12	3.38 ± 0.10
P <sub>8,6</sub> EW	-1.3	-0.9	-1.1	-1.6	-1.2	-3.9	-0.7	-11.6	-2.2	-1.5
P <sub>11,3C</sub>	15.51 ± 1.08	5.46 ± 0.10	6.21 ± 0.15	2.99 ± 0.13	3.82 ± 0.09	2.42 ± 0.04	8.54 ± 0.13	14.71 ± 0.68	10.5 ± 0.07	6.23 ± 0.06
P <sub>11,3C</sub> EW	-3.0	-0.8	-2.1	-8.4	-0.8	-7.6	-1.1	-5.7	-1.1	-2.5
P <sub>12,0</sub> Flux	5.36 ± 0.50	1.39 ± 0.19	2.56 ± 0.23	1.12 ± 0.09	1.47 ± 0.08	0.95 ± 0.09	0.47 ± 0.17	0.95 ± 1.57	2.81 ± 0.11	2.12 ± 0.03
P <sub>12,0</sub> EW	-1.1	-0.2	-0.9	-3.7	-0.3	-3.5	-0.1	-0.3	-0.3	-0.9
P <sub>12,6C</sub> Flux	4.64 ± 0.48	2.59 ± 0.10	3.05 ± 0.37	1.80 ± 0.10	3.01 ± 0.12	2.17 ± 0.14	4.93 ± 0.10	11.66 ± 0.53	4.31 ± 0.06	2.96 ± 0.14
P <sub>12,6C</sub> EW	-1.0	-0.3	-1.2	-7.0	-0.5	-8.9	-0.7	-3.6	-0.4	-1.3
P <sub>13,6</sub> Flux	4.81 ± 0.31	0.12 ± 0.15	1.44 ± 0.35	...	0.69 ± 0.27	0.22 ± 0.09	1.33 ± 0.13	5.57 ± 0.20	...	2.26 ± 0.17
P <sub>13,6</sub> EW	-1.0	0.0	-0.6	...	-0.1	-0.8	-0.2	-1.6	...	-1.1
P <sub>14,2</sub> Flux	2.29 ± 0.18	...	0.11 ± 0.21	...	...	...	2.59 ± 0.08	...	...	...
P <sub>14,2</sub> EW	-0.5	...	-0.1	...	...	...	-0.4	...	...	...
P <sub>16,4</sub> Flux	1.99 ± 0.04	...	...	...	...	...	...	...	...	...
P <sub>16,4</sub> EW	-0.3	...	...	...	...	...	...	...	...	...
P <sub>17C</sub> Flux	9.69 ± 0.17	4.63 ± 2.93	...	...	97.09 ± 0.00	...	...	...	...	...
P <sub>17C</sub> EW	-1.5	-0.4	...	...	-10.3	...	...	...	...	...
P <sub>6,2</sub> /P <sub>7,7</sub>	0.29 ± 0.01	0.65 ± 0.21	0.33 ± 0.03	0.30 ± 0.03	0.46 ± 0.01	0.34 ± 0.06	0.41 ± 0.02	...	0.28 ± 0.01	0.29 ± 0.02
P <sub>11,3</sub> /P <sub>7,7</sub>	0.32 ± 0.02	0.30 ± 0.07	0.28 ± 0.02	0.30 ± 0.03	0.26 ± 0.01	0.31 ± 0.01	0.36 ± 0.02	0.40 ± 0.02	0.25 ± 0.01	0.35 ± 0.01

<sup>a</sup>Flux [W cm<sup>-2</sup>] is scaled by 10<sup>21</sup><sup>b</sup>Fit includes LL spectrum<sup>c</sup>A negative equivalent width [ $\mu$ m] designates line emission.

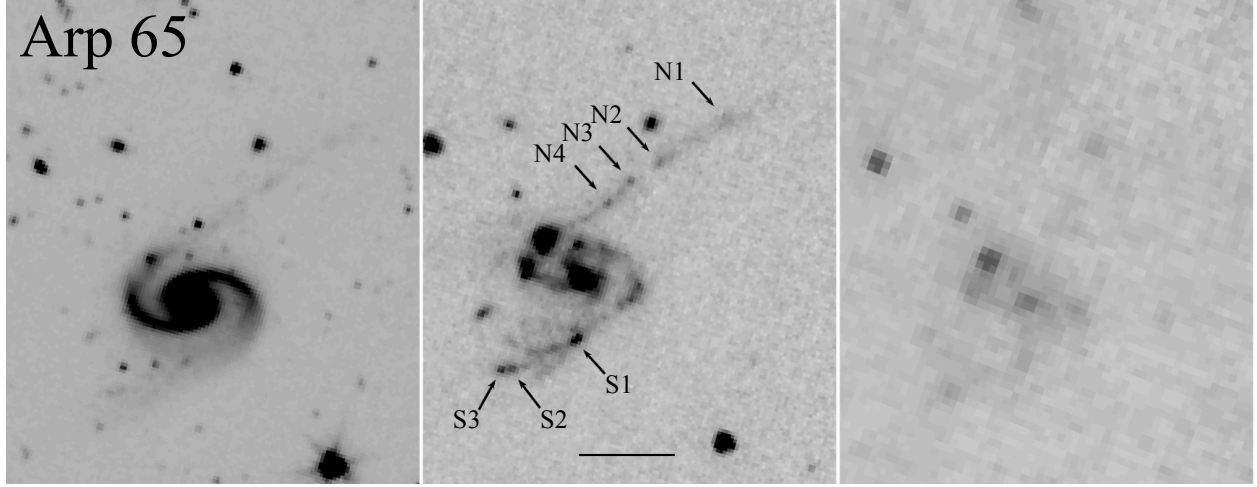


Fig. 1.— Images for the 14 interacting systems, except for NGC 5291 (see HHM06) are displayed in three panels: left-right 3.6, 8.0 & 24  $\mu\text{m}$ . North is at the top and west is to the right. ISFOs are indicated with arrows. A linear transfer function is used in all images, which are displayed on the same scale. A 30'' scalebar is shown in each middle panel. Arp 65 is a widely separated equal mass pair of galaxies. The western galaxy has two tails. The northern tail has beads of star formation terminated with a hinge clump at the base of the tail. The southern tail has an offset between old and young stars (Smith et al. 2007).

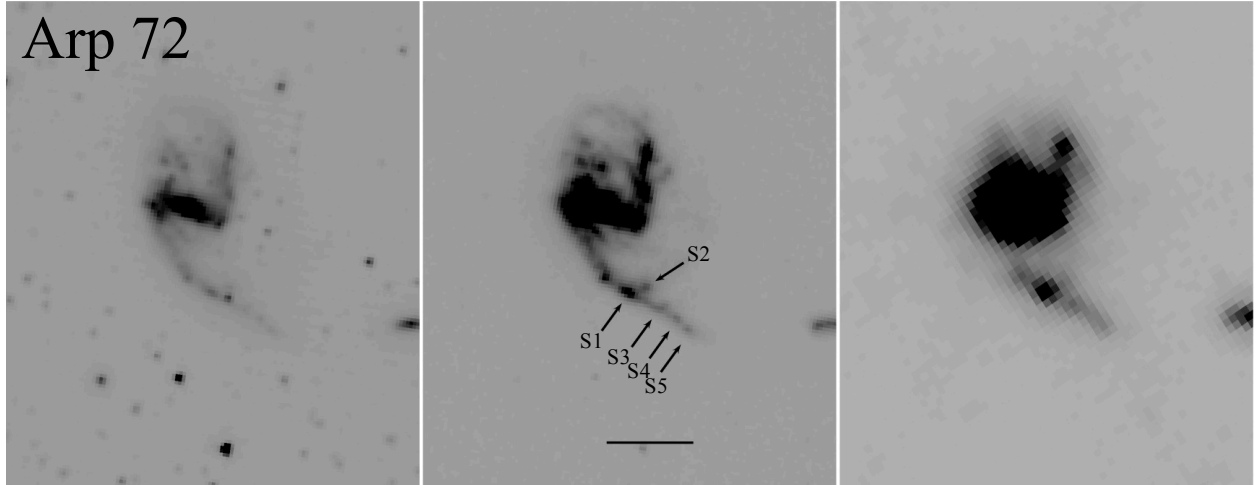


Fig. 1.— Arp 72 consists of the peculiar starburst (NGC 5996) with a strong interaction with its smaller companion NGC 5994. The eastern arm of NGC 5996 is prominent in the UV/visible while the western arm is prominent at both UV/visible wavelengths and at 8  $\mu\text{m}$ . The western arm forms a bridge with the companion. The brightest 8  $\mu\text{m}$  ISFO is in the bridge and is at the base of the bifurcation of the bridge/arm material.

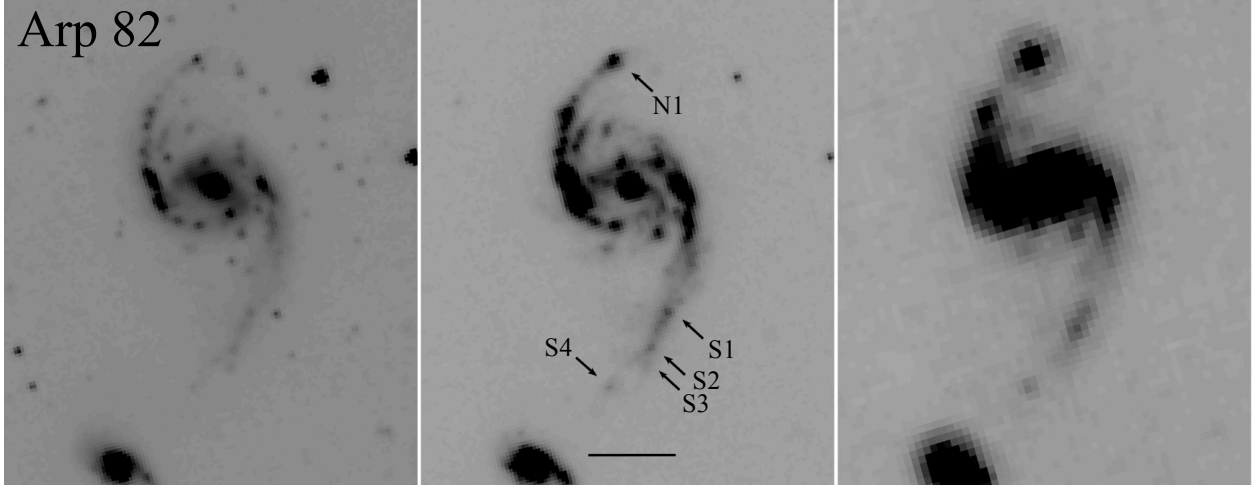


Fig. 1.— cont. Arp 82 is an M51-like system. NGC 2335 is a knotty spiral with a small companion NGC 2536 on the extended southern arm. The southern arm is visible at UV/optical and infrared wavelengths whereas the northern arm is prominent in UV/optical images and absent at  $8\ \mu\text{m}$ . We identify a bright hinge-clump Arp82-N1 at the base of the northern tail. The brightest ISFO in the southern tail is labeled Arp 82-S1.

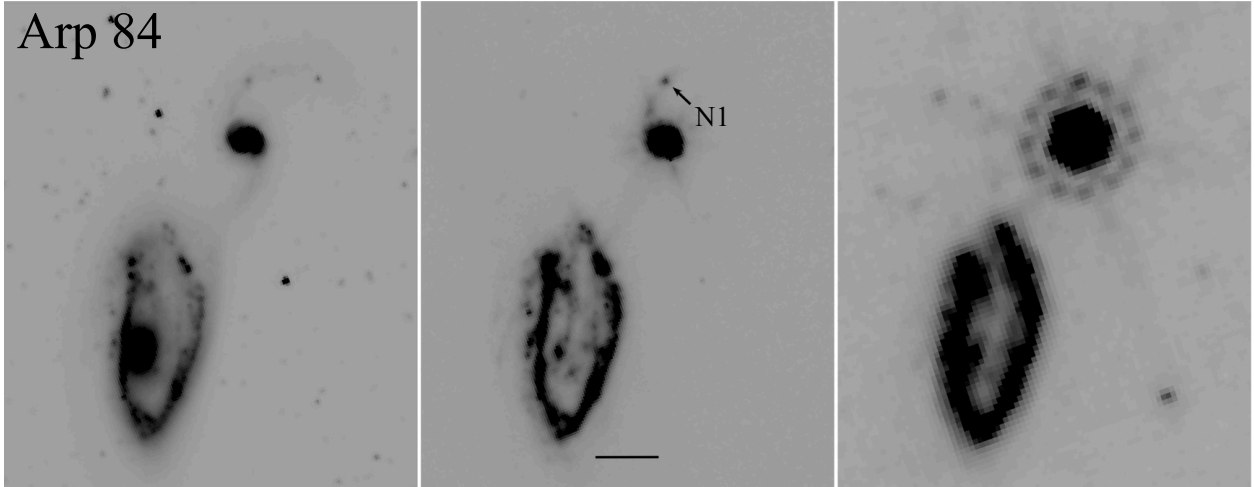


Fig. 1.— cont. Arp 84. NGC 5395 is the large companion and is an asymmetric spiral. NGC 5394 has two open arms. The southern arm connects to NGC 5395. We observed the brightest  $8\ \mu\text{m}$  bead/ISFO in the northern tail. Emission from the ISFO at  $24\ \mu\text{m}$  is confused by diffraction from NGC 3808A. Smith et al. (2007a) note that there may be some accretion material associated with the northern tidal tail.



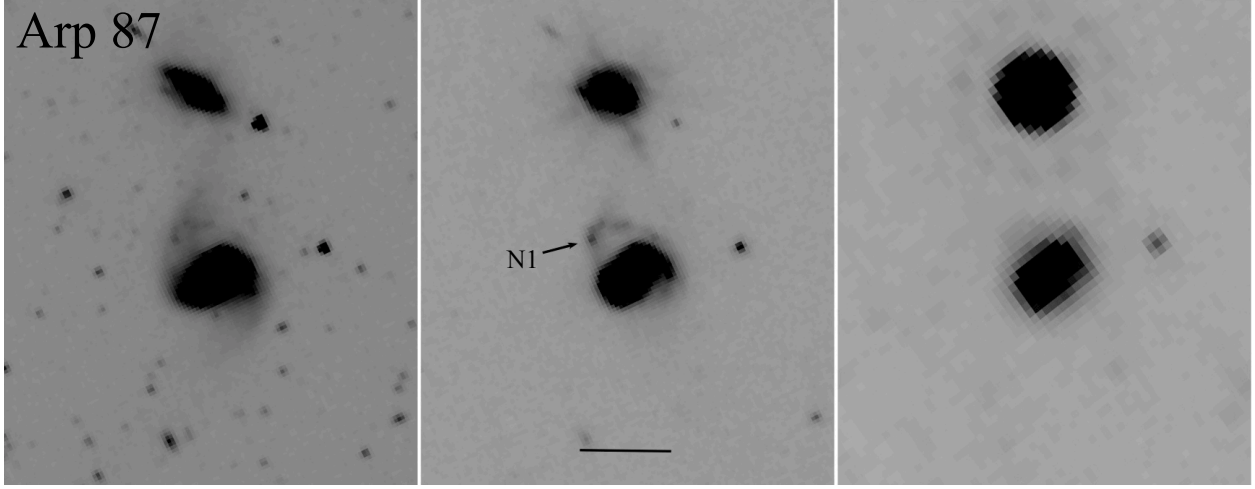


Fig. 1.— cont. Arp 87 is a more equal-mass interacting pair, NGC 3808 and NGC 3808A. NGC 3808 has a polar ring-like structure. We have observed the brightest  $8\ \mu\text{m}$  knot in the bridge star forming region, Arp 87-N1. Emission from the ISFO at  $24\ \mu\text{m}$  is confused by diffraction from the main galaxy.

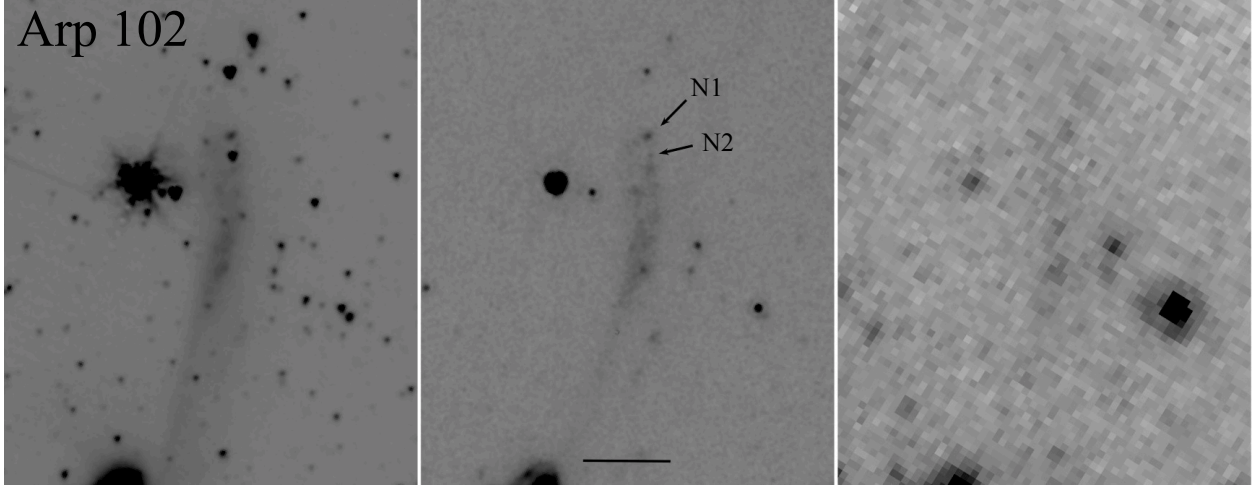


Fig. 1.— cont. Arp 102 is an interaction between a spiral and elliptical galaxy. We imaged the tidal tail to the north of the northern spiral galaxy. Schombert et al. (1990) note that the tail is divided into two by an absorption band and looks like a spiral arm that has been straightened by the interaction between the galaxy pair.

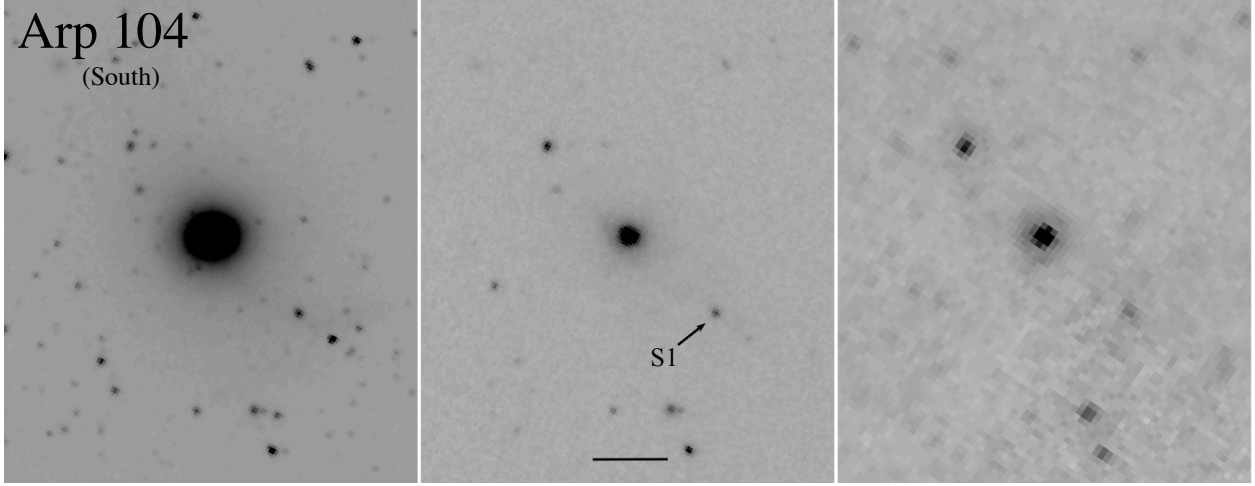


Fig. 1.— cont. Arp 104. NGC 5216 is a peculiar Elliptical connected by an HI bridge to its northern companion (NGC 5218). Arp 104-S1 is at the tip of the tail extending away from NGC 5216.

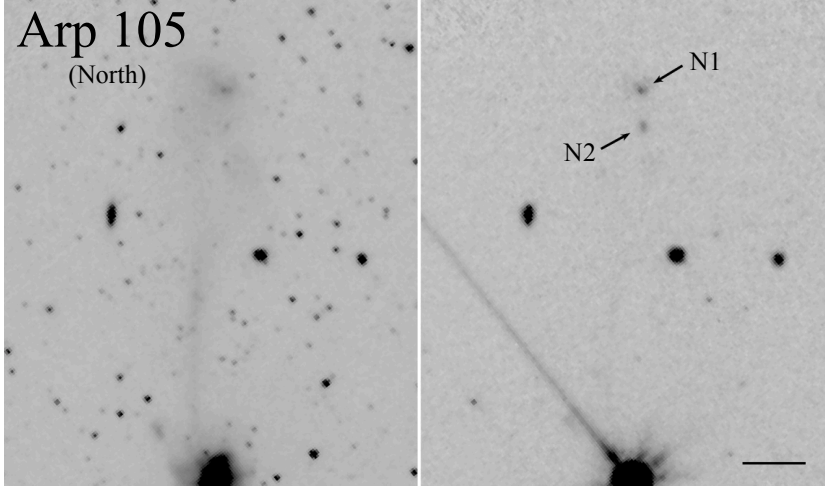


Fig. 1.— cont. Arp 105 North. Arp 105/The Guitar (Abell 1185) consists of a distorted spiral (NGC 3561A) and a very close lenticular companion (NGC 3561B). This figure shows the northern tail. We identify two ISFOs at the tip of this tail. There are no clumps identified along the rest of the 2 arcminute northern tail

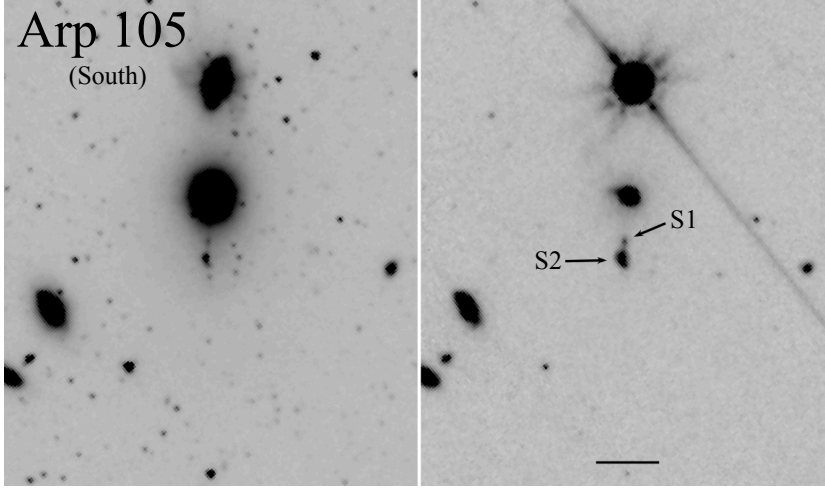


Fig. 1.— cont. Arp 105 South. Smith et al. (2010) considered the southern tail to be an ‘accretion tail’, formed by material from the spiral that fell into the gravitational potential of the elliptical, overshoot that potential, and is now forming stars. Two ISFOs are identified. An analysis of the IRS spectrum of “Ambartsumian’s knot” (S2) at the tip of the short southern tail is presented in this paper.

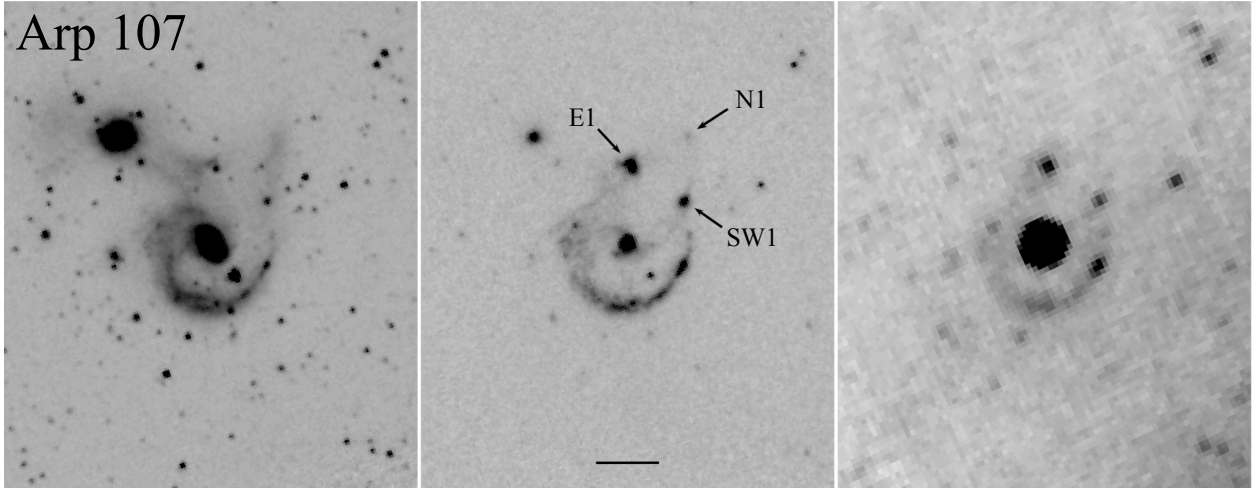


Fig. 1.— cont. Arp 107 has a prominent ring-like structure connected via a bridge to an elliptical-like companion. Smith et al. (2005) reproduced the basic morphology as a collisional ring galaxy with a prograde planar intruder passage. Arp 107-SW1 is at the tip of the southern tail associated with the elliptical-like galaxy.

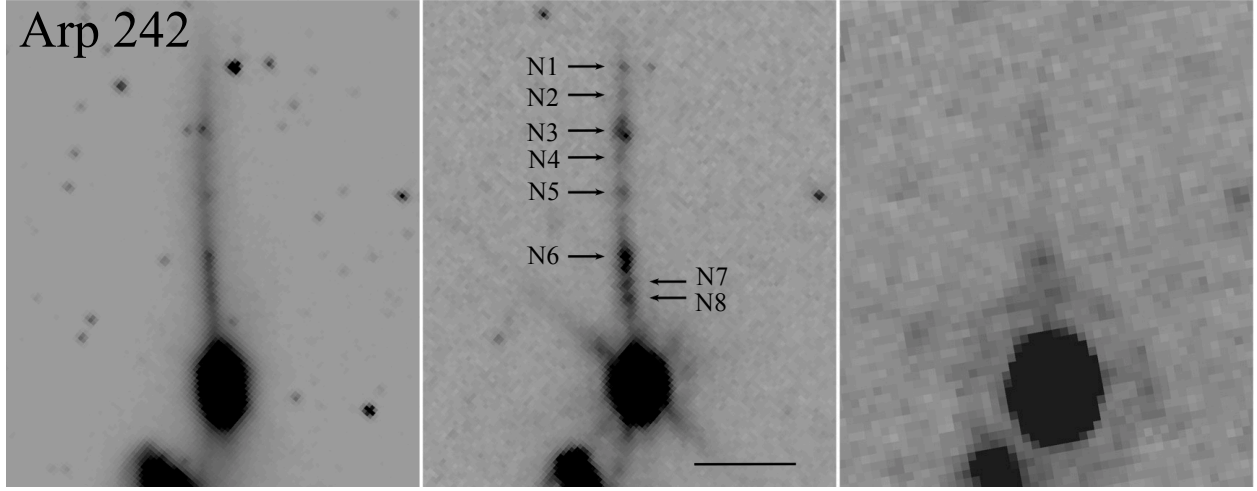


Fig. 1.— cont. Arp 242/Mice/NGC 4676 is a classic example of a tidal interaction between two spirals. Two long tidal tails are visible in the original Arp image (Arp 1966). Only the northern tail is bright at  $8\ \mu\text{m}$ . Arp 242-N3 is the brightest knot in the outer third of the tail.

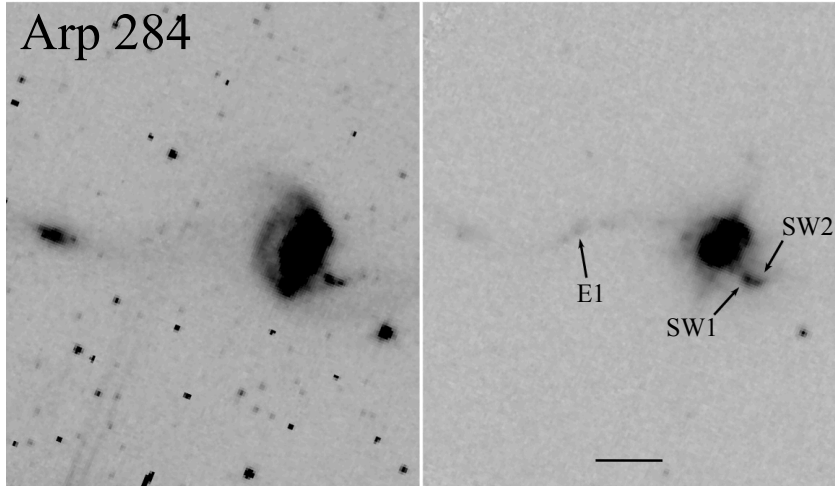


Fig. 1.— cont. Arp 284 consists of two interacting spirals, NGC 7714/5. NGC 7714 is a classic starburst galaxy, with a partial ring with three tails and a bridge connecting it to its edge-on companion NGC 7715. Struck & Smith (2003) reproduced the basic morphology with a pro-grade, near head-on collision, with the western tail being formed via accretion from the bridge and the HI loop being a classical tidal feature. Arp 284-SW1 is a knot in the accretion tail and Arp 284-E1 is a knot in the bridge joining the two galaxies.



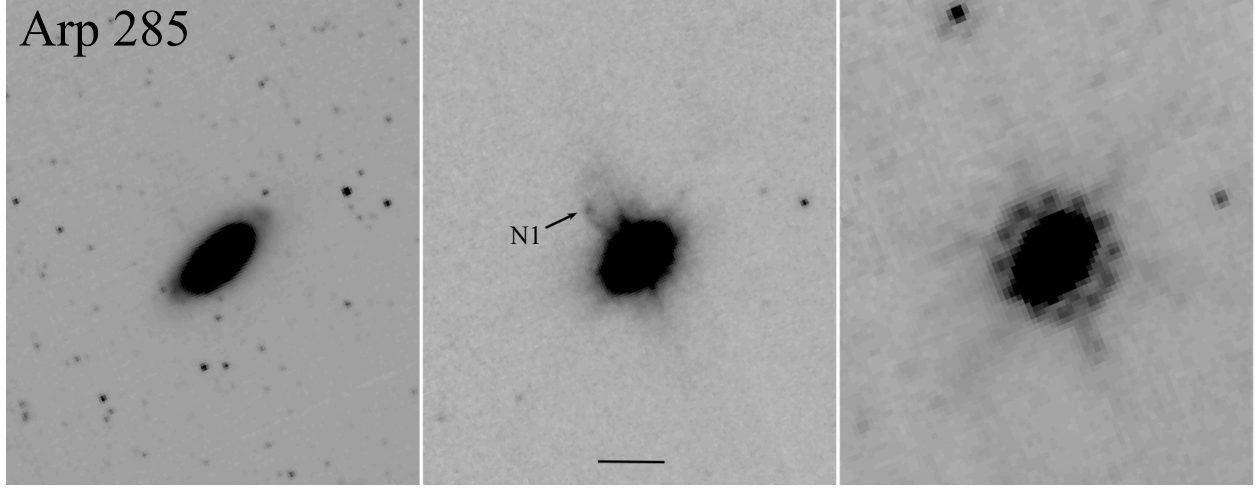


Fig. 1.— cont. Arp 285. The northern tail-like structure is perpendicular to the disk of NGC 2856. Simulations by Smith et al. (2008) suggest this feature may have been accreted from material along the bridge joining NGC 2856 to NGC 2854.

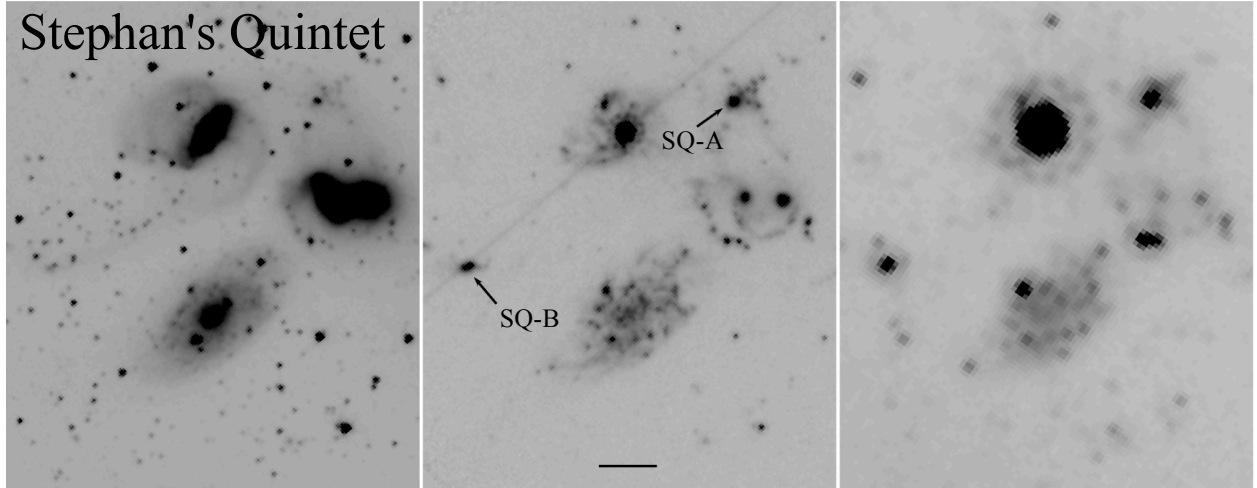


Fig. 1.— cont. Stephan's Quintet (SQ, Arp 319) is a prototype compact group (Hickson 92). There are five galaxies in SQ: NGC 7317(E), NGC 7318A(E), NGC 7318B (Sbc pec), NGC 7319 (Sbc pec Sey 2) and NGC 7320 (Sd foreground galaxy). Two 100 kpc parallel tails stretch from NGC 7319 towards the intruder NGC 7320c. We observed SQ-A with the IRS. (spectra are not included for SQ-B (Arp 1973) in the tidal tail of NGC7319/HCG 92C, due to a pointing issue with the data).

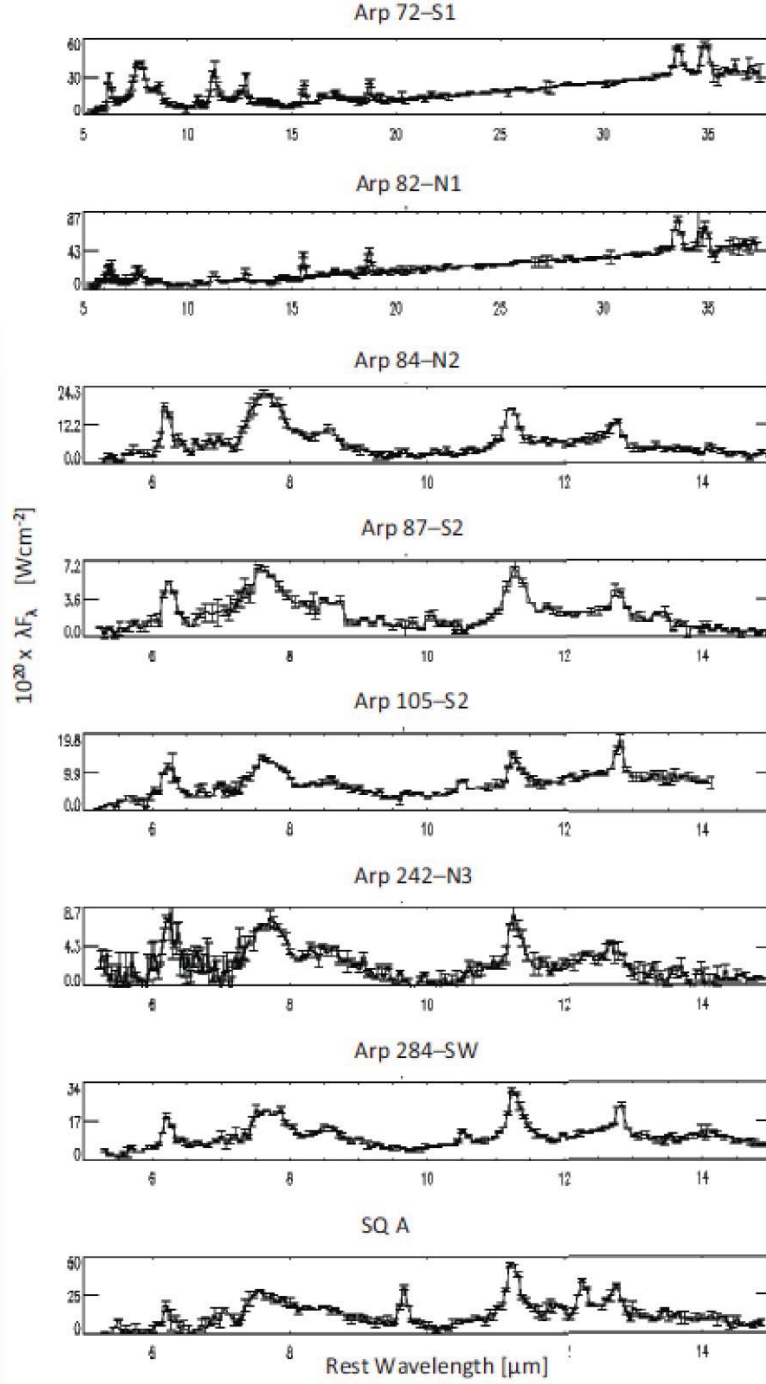


Fig. 2.— IRS LORES Spectra. Note, the spectra of Arp 72-S1 & Arp 82-N1 include IRS-LL data.

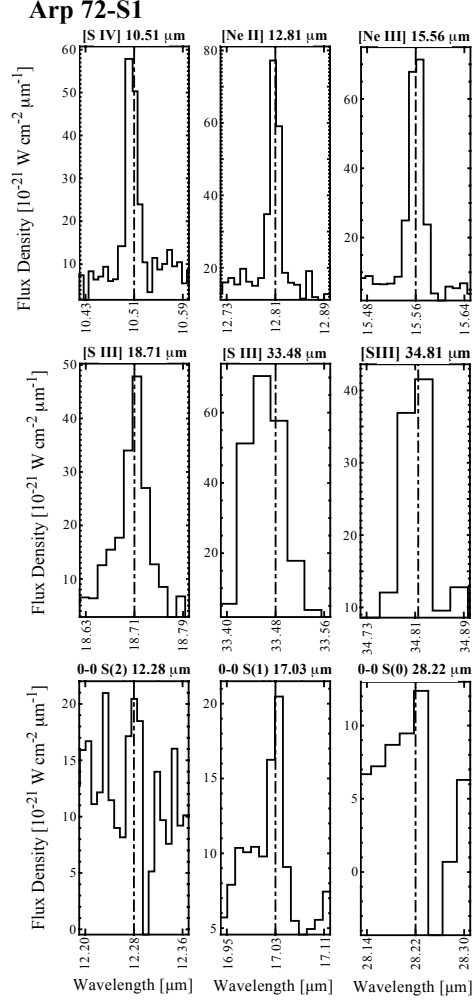


Fig. 3.— IRS HIRES emission line profiles - Arp 72-S1

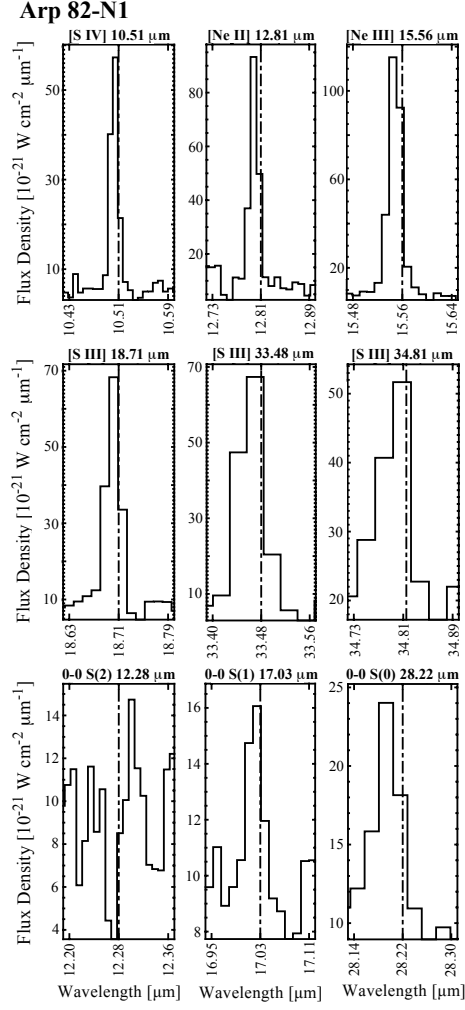


Fig. 3.— cont. Arp 82-N1



**Arp 84-N1**

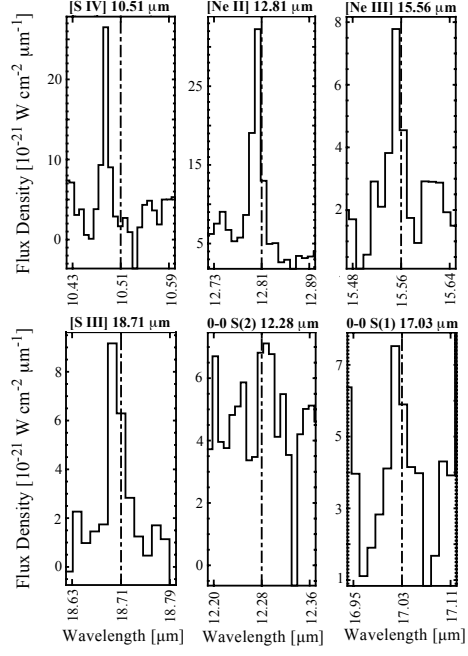


Fig. 3.— cont. Arp 84-N1

**Arp 87-N1**

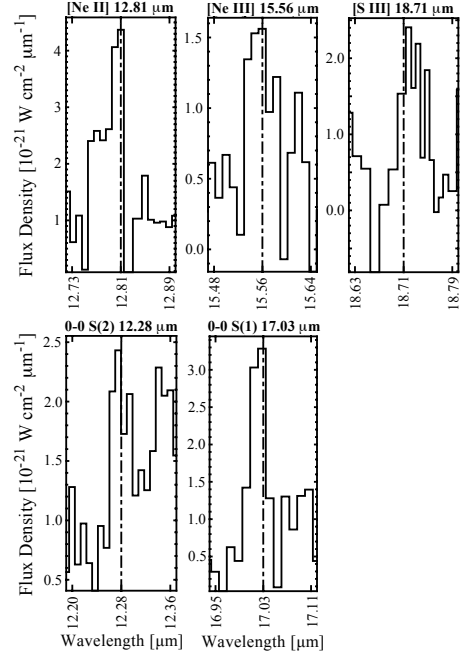


Fig. 3.— cont. Arp 87-N1

**Arp 284-SW1**

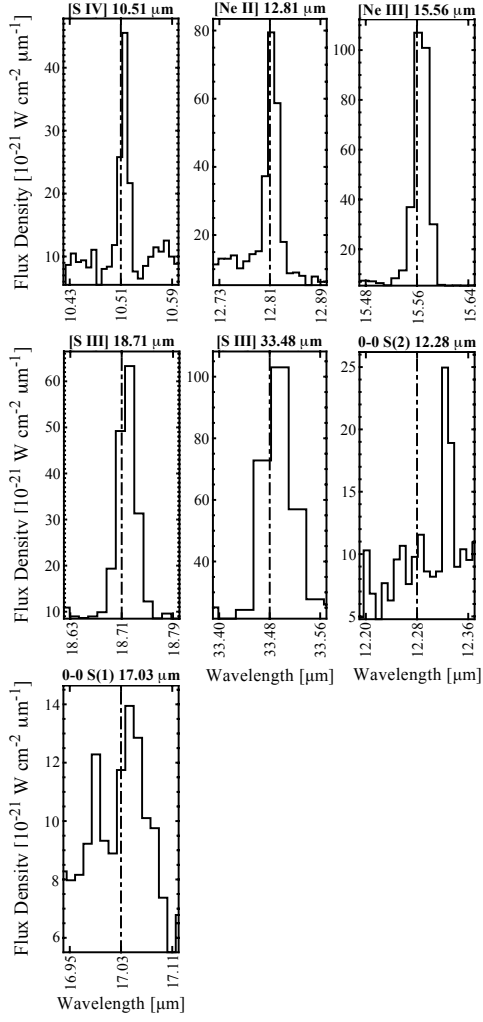


Fig. 3.— cont. Arp 284-SW1

**SQ A**

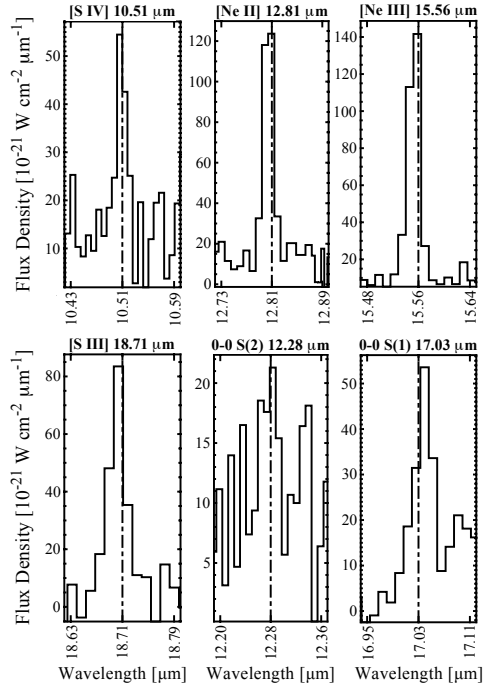


Fig. 3.— cont. SQ A

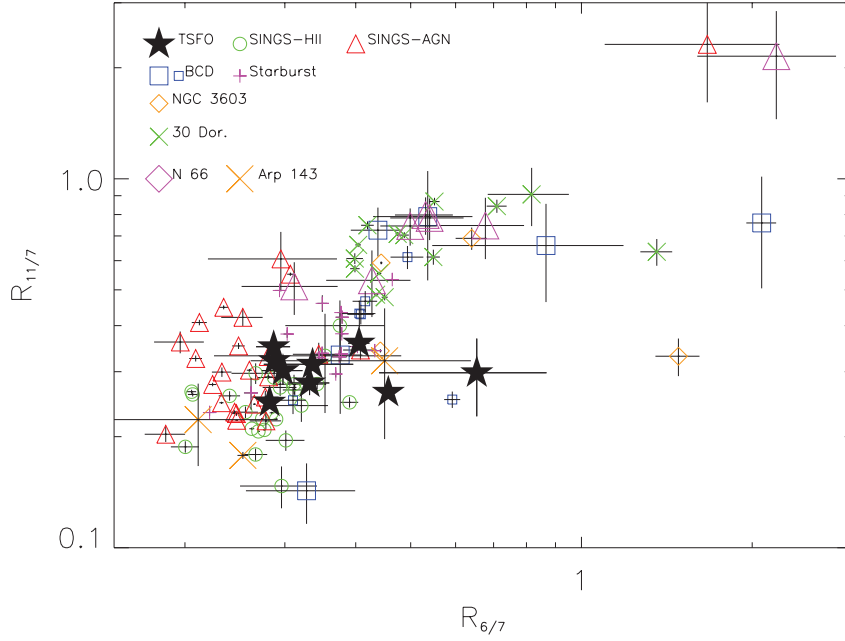


Fig. 4.— Relative strengths of the PAH bands.  $R_{11/7}$  increases with decreasing PAH ion fraction and  $R_{6/7}$  increases with decreasing PAH size. ISFOs are shown as filled stars. The SINGS-AGN are shown as (red) open triangles and the SINGS-HII (green) open circles (Smith et al. 2007b). BCDs are shown as (blue) large open squares (Hunt et al. 2010). Clumps in Arp 143 are shown as (orange) large X’s (Beiraro et al. 2009). Star forming regions in NGC 3603 in the Milky Way are shown as (orange) open diamonds, in 30 Dor. in the LMC as (green) small x’s and in N 66 in the SMC as (pink) large open triangles, BCDs (blue) small open squares, starburst galaxies (pink) pluses (Lebouteiller et al. 2011). A color version of this figure is available in the online journal.

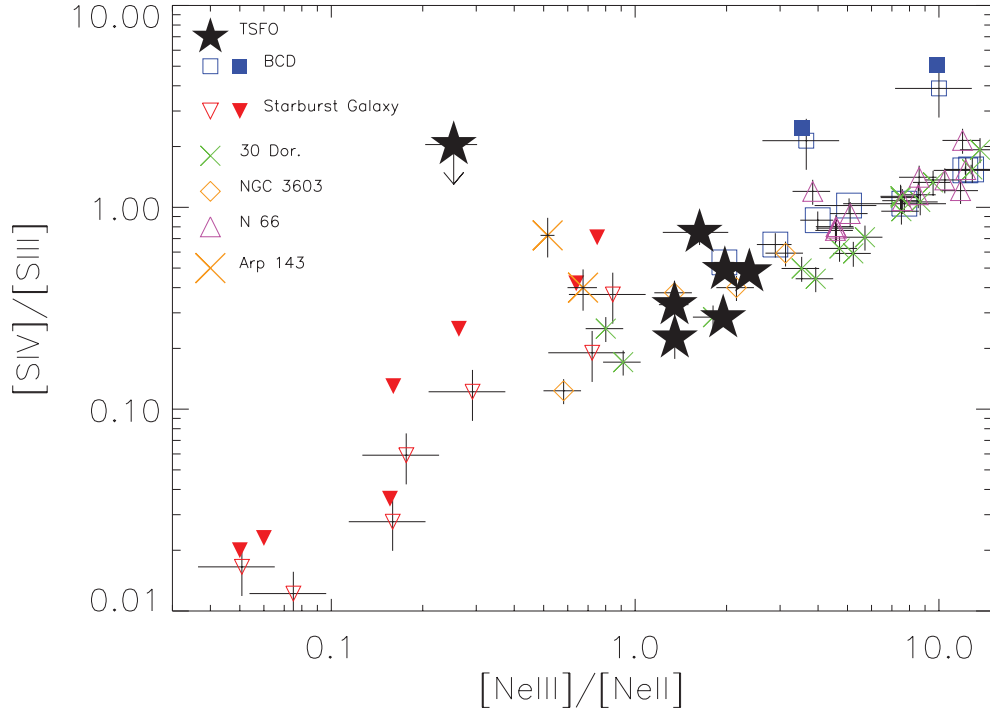


Fig. 5.— Mid-infrared excitation diagram. ISFOs are displayed with a filled star symbol. Dusty starbursts are shown as (red) open inverted triangles, and extinction corrected data as (red) filled inverted triangles; BCDs are shown as (blue) small open squares and filled squares (extinction corrected, Verma et al. 2003. We adopted a 20% uncertainty in the line fluxes). Additional BCDs are displayed as (blue) large open squares (Hunt et al. 2010). Star forming regions in 30 Dor, NGC 3603 and N 66 are displayed using the same symbols as in Figure 4. The ISFOs are assumed to have minimal extinction ( $A_V \leq 3$ ) and the line ratios are not corrected. A color version of this figure is available in the online journal.

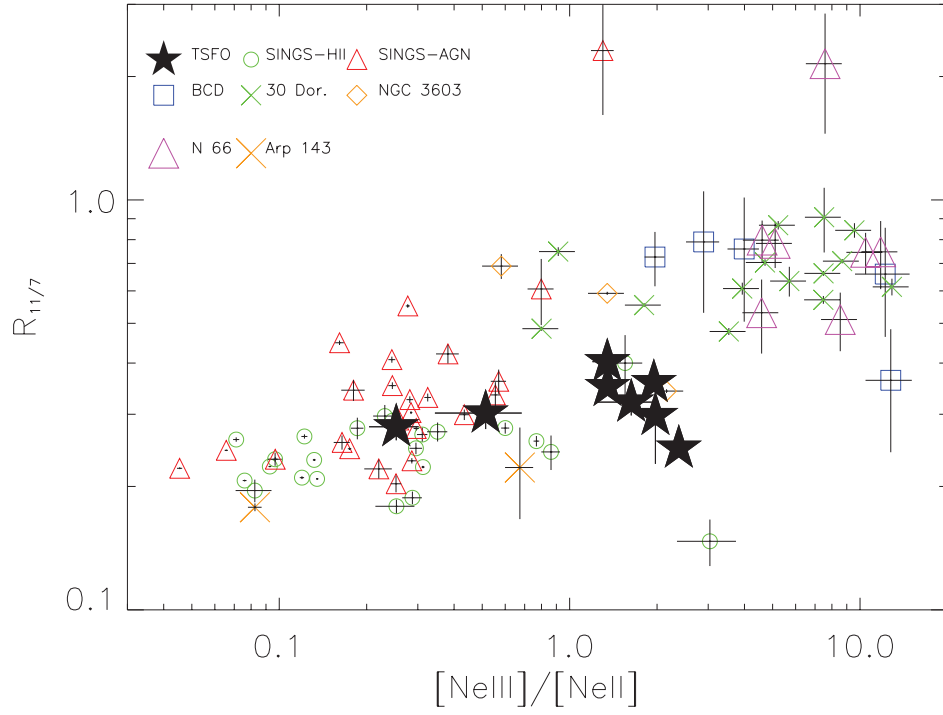


Fig. 6.—  $R_{11/7}$  as a function of the hardness of the ISRF as measured by the  $[\text{Ne III}]/[\text{Ne II}]$  line flux ratio. Symbols are the same as for Figure 4. The ISFOs display no significant increase in  $R_{11/7}$  when the neon line ratio is  $>1$ . A color version of this figure is available in the online journal.

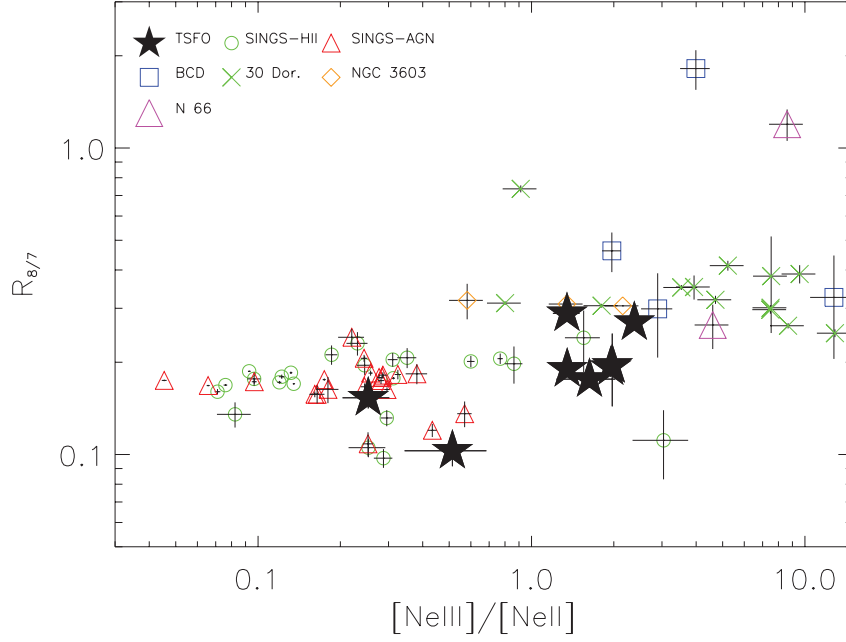


Fig. 7.—  $R_{8/7}$  as a function of the hardness of the ISRF as measured by the [Ne III]/[Ne II] line flux ratio. Symbols are the same as for Figure 5. A color version of this figure is available in the online journal.

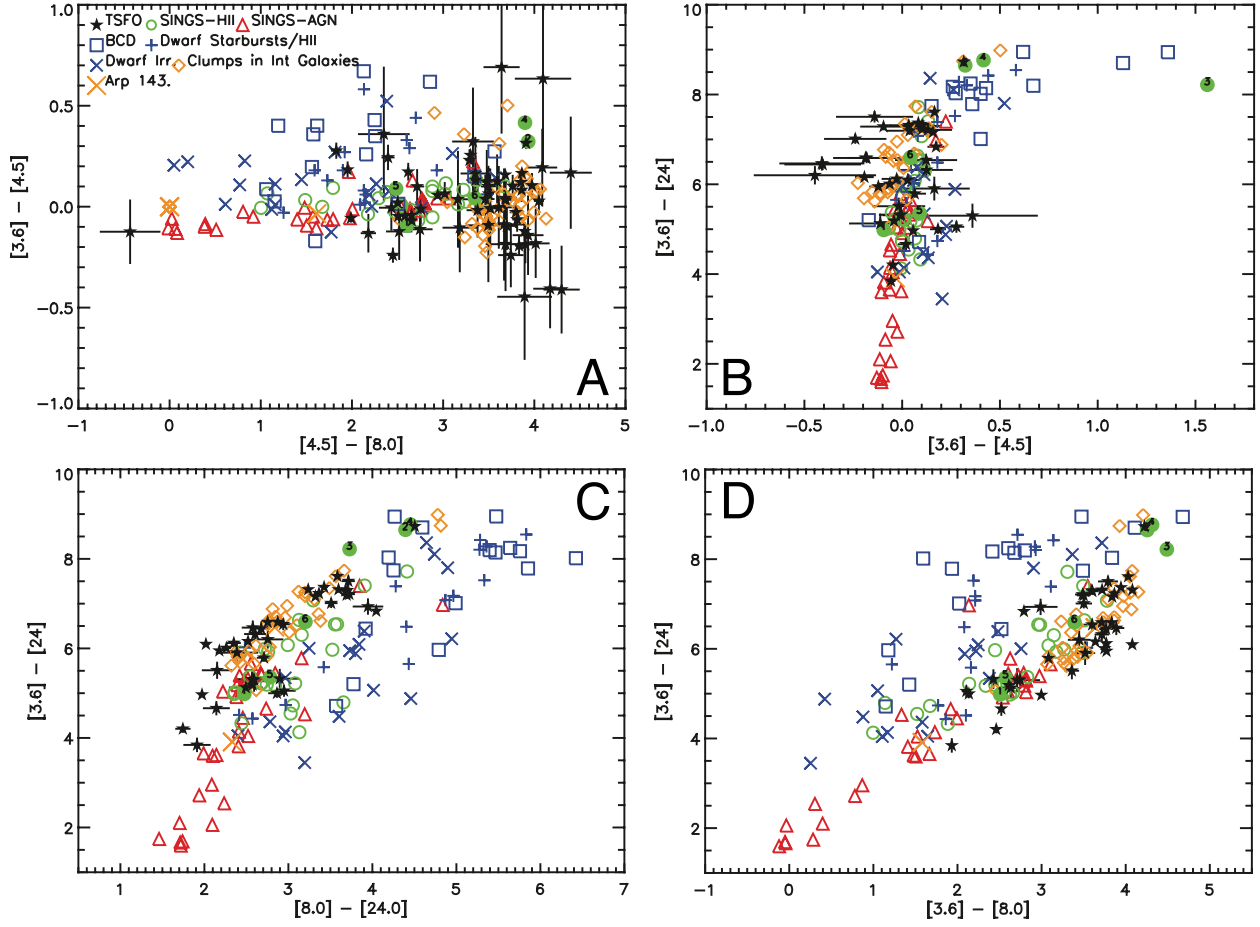


Fig. 8.— Spitzer Two-Color Diagrams. The ISFOs are shown as filled stars, while the SINGS-HII are shown as (green) open circles, SINGS-AGN are shown as (red) open triangles. A sample of dwarf galaxies (Smith & Hancock 2009) are shown as (blue) open squares (BCDs), (blue) pluses (starburst/HII), and (blue) Xs (irregular). A selection of clumps from the inner disks of interacting systems are shown as (orange) open diamonds (Lapham et al. 2013 and references therein). Data is shown for regions in Arp 24, Arp 82, Arp 244, Arp 284 & Arp 285. Data for Arp 143 is shown as large (orange) X’s (Beiraro et al. 2009). Template colors for discrete sources identified in M 33 (Verley et al. 2007) are numbered (green solid circles): (1) PNe, (2) HII (infrared sample), (3) HII (radio sample), (4) HII (optical sample), (5) SNR, (6) Unknown source type. For clarity only the uncertainties for the ISFOs are shown. The very blue  $[4.5] - [8.0]$  ISFO in the far left of Panel (A) is most likely a background elliptical galaxy. A color version of this figure is available in the online journal.



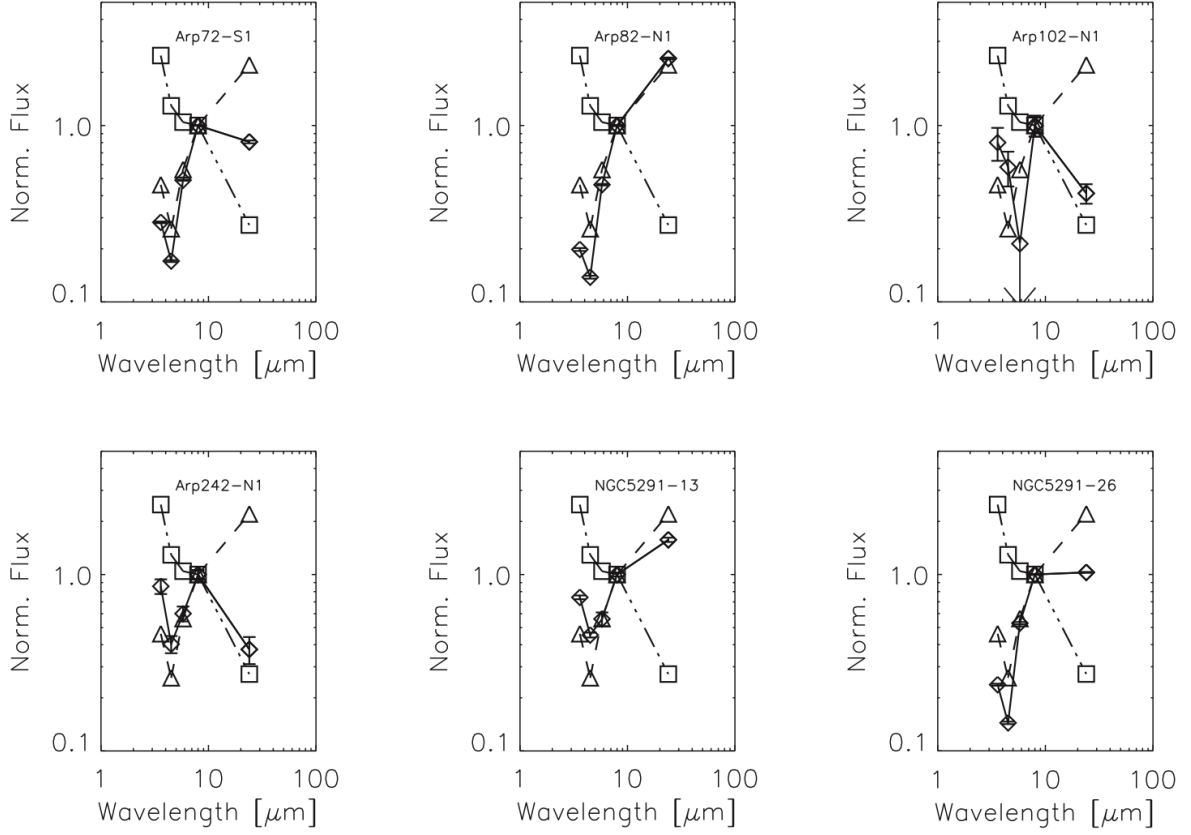


Fig. 9.— A selection of ISFO SEDs shown as diamond symbols. Overlaid are two galaxy SEDs from Draine et al. (2007), which serve as templates for regions dominated by emission from dust in the diffuse ISM (NGC 3190) shown with square symbols and from dust in PDRs (Mrk 33) shown with triangles. Each data set has been normalized to the 8  $\mu\text{m}$  flux ( $\lambda F_{\lambda}(8\mu\text{m}) = 1$ ).